Chapter 11
Kinetics and Mechanisms of Reduction of Protons and Carbon Dioxide Catalyzed by Metal Complexes and Nanoparticles

Shunichi Fukuzumi, Tomoyoshi Suenobu, and Yusuke Yamada

Abstract Kinetics and mechanisms of reduction of protons and CO_2 catalyzed by metal complexes and nanoparticles have been discussed in this chapter. Kinetic studies including deuterium kinetic isotope effects on heterogeneous catalysts for hydrogen evolution by proton reduction have been demonstrated to provide essential mechanistic information on bond cleavage and formation associated with electron transfer. The rate-determining steps in the catalytic cycles are clarified by kinetic studies, providing valuable information on observable intermediates. The most important intermediates in the catalytic reduction of protons and CO_2 are metal-hydride complexes, which can reduce protons and CO_2 to produce hydrogen and formic acid, respectively. The catalytic interconversion between hydrogen and a hydrogen storage compound has been made possible by changing pH, providing a convenient hydrogen-on-demand system in which hydrogen gas can be stored as a liquid (e.g., formic acid) or solid form (NADH) and hydrogen can be produced by the catalytic decomposition of the hydrogen storage compound.

Keywords Proton reduction • CO_2 reduction • Metal hydride • Kinetics • Nanoparticles

11.1 Introduction

The global annual energy consumption is increasing rapidly, whereas fossil fuels, which are currently the primary source of the energy, will be depleted eventually in the future. In addition, the burning of fossil fuels releases large amounts of carbon dioxide (CO_2) to the atmosphere, leading to global warming. Before the depletion of fossil fuels, which are the products of photosynthesis, artificial photosynthesis should be realized to produce solar fuels and to fix CO_2 using solar energy, which is

---

S. Fukuzumi (✉) • T. Suenobu • Y. Yamada
Department of Material and Life Science, Division of Advanced Science and Biotechnology, Graduate School of Engineering, Osaka University, ALCA, Japan Science and Technology Agency (JST), Suita, Osaka 565-0871, Japan
e-mail: fukuzumi@chem.eng.osaka-u.ac.jp

W.-Y. Wong (ed.), *Organometallics and Related Molecules for Energy Conversion*,
Green Chemistry and Sustainable Technology, DOI 10.1007/978-3-662-46054-2_11

the most abundant on the earth [1–4]. In an ideal artificial photosynthesis, water is split using solar energy into hydrogen (H_2) and dioxygen (O_2), which in turn can be converted into water releasing its energy as electricity in H_2 fuel cells [5–10]. Once H_2 is formed from water, CO_2 can be reduced by H_2 to produce carbon monoxide or formate, which can be further reduced to methanol and methane [11–16]. Such reduction of CO_2 by H_2 provides the possibility of storing solar energy as these C1 compounds, contributing to reduced emission of CO_2. There have so far been many reviews on each step of artificial photosynthesis, i.e., light harvesting and charge separation [17–23], proton reduction [24–28], CO_2 reduction [29–33], and water oxidation [34–42]. However, the detailed catalytic mechanisms of reduction of protons for hydrogen evolution and reduction of CO_2 have yet to be fully clarified. Kinetic studies certainly help in understanding catalytic mechanisms of proton reduction and CO_2 reduction, which are catalyzed by metal complexes and nanoparticles. Thus, in this review, we have chosen to focus on kinetics and mechanisms of reduction of protons and CO_2 catalyzed by metal complexes and nanoparticles.

11.2 Mechanisms of Catalytic Hydrogen Evolution

11.2.1 Cobalt Hydride Complexes

Platinum is currently used as the most efficient catalyst for the reduction of protons to H_2 [43]. Because of the scarcity and high cost of platinum, replacement of platinum by more earth-abundant metals such as cobalt as proton reduction catalysts has attracted much attention [44–48]. In order to develop efficient proton reduction catalysts, it is quite important to elucidate mechanisms of the catalytic proton reduction. The mechanism of the proton reduction by Co complexes has been clarified using a dinuclear Co complex with bis(pyridyl)pyrazolato (bpp^-) and terpyridine (trpy) ligands, $[Co^{III}_2(trpy)_2(\mu\text{-bpp})(OH)(OH_2)](PF_6)_4$($\mathbf{1}(PF_6)_4$, Fig. 11.1) [49].

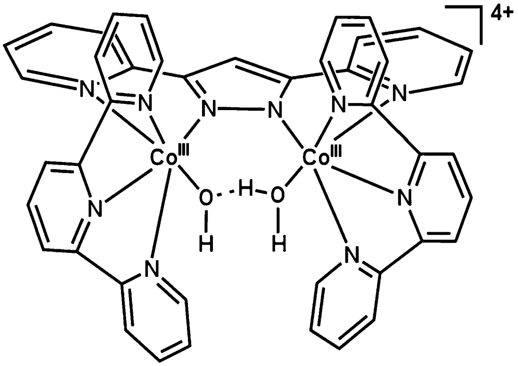

Fig. 11.1 Structure of $[Co^{III}_2(trpy)_2(\mu\text{-bpp})(OH)(OH_2)]^{4+}$ ($\mathbf{1}^{4+}$)

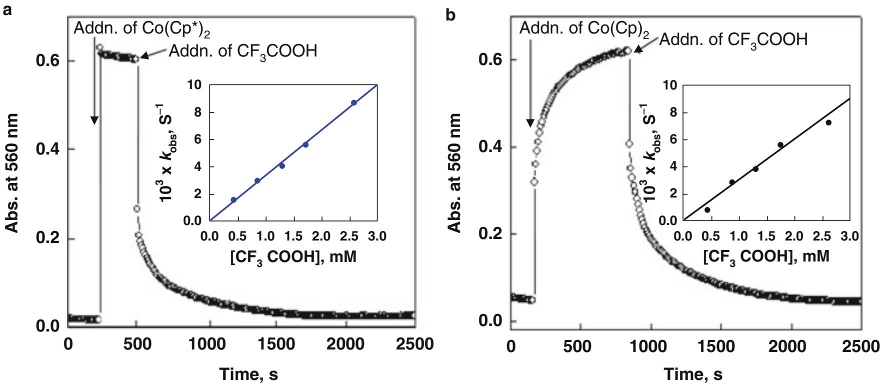

Fig. 11.2 Time profiles of absorbance at 560 nm due to (**a**) the $Co^{I}Co^{I}$ complex (**1**, 0.087 mM) and (**b**) the $Co^{II}Co^{I}$ complex ($\mathbf{1}^+$, 0.087 mM) with CF_3COOH (0.87 mM) in deaerated MeCN at 298 K. *Insets*: Plots of k_{obs} vs. concentration of CF_3COOH for the second step reaction of (**a**) **1** and (**b**) $\mathbf{1}^+$ with CF_3COOH (Reprinted with the permission from Ref. [49]. Copyright 2011 American Chemical Society)

The dinuclear cobalt(III) complex ($\mathbf{1}^{4+}$) undergoes step-by-step reduction by decamethylcobaltocene ($Co(Cp^*)_2$, $Cp^* = \eta^5$-pentamethylcyclopentadienyl) to **1**, because the one-electron oxidation potential of $Co(Cp^*)_2$ ($E_{ox} = -1.53$ V vs. SCE) is lower than the one-electron reduction potential of $\mathbf{1}^+$ ($E_{red} = -1.09$ V vs. SCE) [49]. Addition of 4 equiv. of $Co(Cp^*)_2$ to a deaerated MeCN solution containing $\mathbf{1}^{4+}$ resulted in rapid formation of **1**, which exhibits visible and NIR absorption bands at 560 and 1,050 nm [49]. Addition of 10 equiv. of CF_3COOH to the MeCN solution of **1** resulted in the two-step decay of absorbance at 560 nm due to **1** (Fig. 11.2a) [49]. The two-step reaction of **1** with CF_3COOH suggests that the protonation of **1** affords a hydride complex, $[(Co^{III}–H)(Co^{III}–H)]^{2+}$, which is in equilibrium with **1**, followed by the reaction of the hydride complex with protons to produce H_2 [49]. The first-order dependence of k_{obs} with respect to the concentration of CF_3COOH in the second step indicates that the protonation of the Co(III)–H moiety is the rate-determining step to produce H_2 [49].

When cobaltocene ($Co(Cp)_2$, $Cp = \eta^5$-cyclopentadienyl) was used as a reductant, $\mathbf{1}^+$ was obtained by the three-electron reduction of $\mathbf{1}^{4+}$ with $Co(Cp)_2$, because the one-electron oxidation potential of $Co(Cp)_2$ ($E_{ox} = -0.9$ V vs. SCE) is more negative than the E_{red} value of $\mathbf{1}^{2+}$ (−0.78 V vs. SCE) but less negative than the E_{red} value of $\mathbf{1}^+$ (−1.09 V vs. SCE) [49]. The reaction of $\mathbf{1}^+$ with CF_3COOH also exhibited a two-step decay (Fig. 11.2b) [49].

Based on the two-step kinetics, the reaction mechanism of H_2 production from $\mathbf{1}^+$ is shown in Scheme 11.1 [49]. Three-electron reduction of $\mathbf{1}^{4+}$ by 3 equiv. of Co $(Cp)_2$ occurs to produce $\mathbf{1}^+$ (Eq. 11.1). $\mathbf{1}^+$ is protonated by CF_3COOH to produce the hydride complex ($[Co^{II}Co^{III}–H]^{2+}$), which is in equilibrium with $\mathbf{1}^+$ (Eq. 11.2, the first step in Fig. 11.2b). The formation of hydride complex was confirmed by the ^1H NMR spectra which exhibit a typical Co(III)–H peak at $\delta = -8.64$ ppm [49]. The

Scheme 11.1 Reaction mechanism of H_2 production with $[Co^{II}Co^{I}]^+$

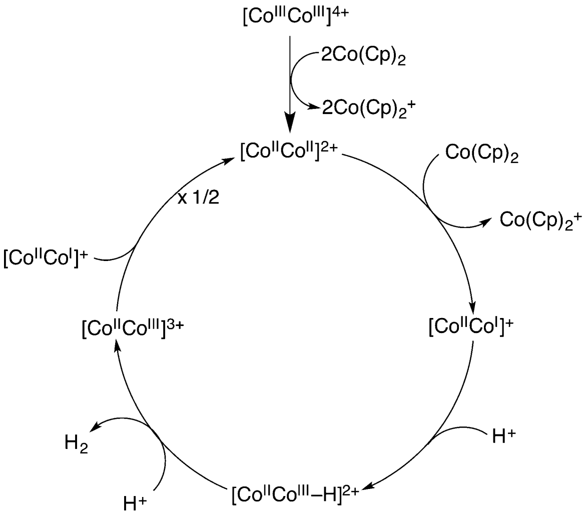

hydride complex reacts with protons to produce H_2 and $\mathbf{1}^{3+}$ (Eq. 11.3). This is the rate-determining step for the H_2 production, because the k_{obs} values for the second step are proportional to the proton concentration (inset of Fig. 11.2b) [49]. $\mathbf{1}^{3+}$ is reduced by $\mathbf{1}^{+}$ to produce two equivalent $\mathbf{1}^{2+}$ (Eq. 11.4) [49]:

$$\left[Co^{III}Co^{III}\right]^{4+} + 3Co(Cp)_2 \rightarrow \left[Co^{II}Co^{I}\right]^{+} + 3Co(Cp)_2^{+} \tag{11.1}$$

$$\left[Co^{II}Co^{I}\right]^{+} + H^{+} \rightleftharpoons \left[Co^{II}Co^{III} - H\right]^{2+} \tag{11.2}$$

$$\left[Co^{II}Co^{III} - H\right]^{2+} + H^{+} \rightarrow \left[Co^{II}Co^{III}\right]^{3+} + H_2 \tag{11.3}$$

$$\left[Co^{II}Co^{I}\right]^{+} + \left[Co^{II}Co^{III}\right]^{3+} \rightarrow 2\left[Co^{II}Co^{II}\right]^{2+} \tag{11.4}$$

$$-d\left[\left[Co^{II}Co^{I}\right]^{+}\right]/dt = k[H^{+}]\left[\left[Co^{II}Co^{I}\right]^{+}\right]/(1 + K[H^{+}]) \tag{11.5}$$

According to Scheme 11.1, the rate of decay of $\mathbf{1}^{+}$ is given by Eq. 11.5, where k is the rate constant of protonation of the hydride complex to produce H_2 (Eq. 11.3) and K is the protonation equilibrium constant of $\mathbf{1}^{+}$ to produce the hydride complex, $[Co^{II}Co^{III}–H]^{2+}$ (Eq. 11.2). Based on the kinetic results in Fig. 11.2, the k and K values of $\mathbf{1}^{+}$ at 298 K were determined to be 2.9 M^{-1} s^{-1} and 5.3×10^2 M^{-1}, respectively [49]. Similarly the k and K values of **1** at 298 K were also determined to be 3.3 M^{-1} s^{-1} and 1.1×10^3 M^{-1}, respectively [49]. The K value of **1** is twice larger than that of $\mathbf{1}^{+}$, because **1** has two Co^{I} sites as compared with $\mathbf{1}^{+}$ which has one Co^{I} site. The similar k values between $\mathbf{1}^{+}$ and **1** suggest that the two Co^{I} sites in **1** act rather independently in the reaction with proton.

A cobalt tetraaza-macrocyclic complex $[Co^{III}(CR)Cl_2]^+$ (CR = 2,12-dimethyl-3,7,11,17-tetraazabicyclo(11.3.1)-heptadeca-1(17),2,11,13,15-pentaene) has been

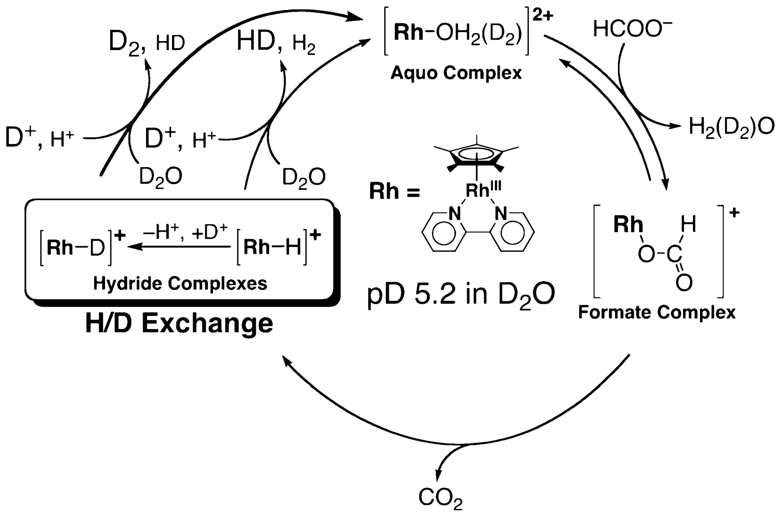

Scheme 11.2 Catalytic mechanism of decomposition of HCOOH by **2** in D_2O

reported to act as an efficient proton reduction catalyst in photocatalytic hydrogen evolution with ascorbate (HA^-) and ascorbic acid (H_2A) as an electron donor and a proton donor, respectively, and $[Ru(bpy)_3]^{2+}$ as a photocatalyst in water [50]. The catalytic activity and stability of $[Co^{III}(CR)Cl_2]^+$ were higher than that of other cobalt complexes such as cobaloxime derivatives [51–53] to afford a high turnover number (TON = 1,000) [50]. The Co(III) complex was reduced with HA^- to produce the Co(II) complex [50]. The Co(II) complex was further reduced by electron transfer from the excited state of $[Ru(bpy)_3]^{2+}$ ($[Ru(bpy)_3]^{2+*}$ where * denotes the excited state) to produce the Co(I) complex, which reacts with protons to yield H_2 and the Co(II) complex similar to $\mathbf{1}^+$ in Scheme 11.1 [50]. In this case, however, formation of the Co(III)-hydride complex has not been detected [50]. The detailed photocatalytic mechanism of hydrogen evolution is discussed in the next section.

11.2.2 Rhodium Hydride Complexes

A water-soluble rhodium-aqua complex, $[Rh^{III}(Cp^*)(bpy)(H_2O)](SO_4)$ (**2**(SO_4), bpy = 2,2′-bipyridine), acts as an efficient catalyst for H_2 evolution from HCOOH in an aqueous solution at 298 K [54]. The kinetic study revealed the catalytic mechanism of the catalytic decomposition of HCOOH to H_2 and CO_2 with **2** (SO_4) as shown in Scheme 11.2 [54]. The rate of H_2 evolution increased linearly with increasing concentrations of **2**(SO_4) as shown in Fig. 11.3a. On the other hand, the TOF value increased with increasing [HCOOH] to reach a limiting value as shown in Fig. 11.3b. Such a saturation behavior indicates that the formation of the formate complex is in equilibrium with $HCOO^-$, followed by β-hydrogen

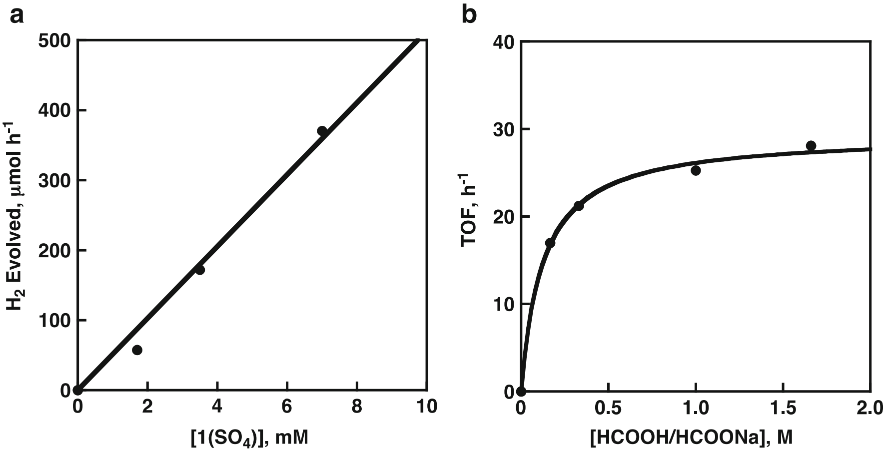

Fig. 11.3 (**a**) Plot of rate of H_2 evolution vs. the concentration of **2**(SO_4) in the decomposition of HCOOH/HCOONa (1.7 M) catalyzed by **2**(SO_4) in deaerated H_2O at pH 4.1 at 293 K. (**b**) Plot of TOFs vs. the concentration of HCOOH/HCOONa in the decomposition of HCOOH/HCOONa catalyzed by **2**(SO_4) (7.0 mM) in deaerated H_2O at pH 3.8 at 298 K (Reproduced from Ref. [54] by permission of John Wiley & Sons Ltd)

elimination from the formate complex to produce the Rh^{III}-hydride complex, which becomes the rate-determining step at large concentrations of $HCOO^-$. The formate complex ($[Rh^{III}(Cp^*)(OC(O)H)(bpy)]^+$) was detected by the electrospray ionization (ESI)-mass spectrometry at $m/z = 439.2$ [54]. When pH was changed, the maximum TOF value was obtained at pH 3.9, which corresponds to pK_a of HCOOH. No catalytic reactivity was observed at pH higher than pK_a of **2**(SO_4), indicating that the hydroxo complex $[Rh^{III}(Cp^*)(OH)(bpy)]^+$ has no catalytic reactivity [54].

When HCOOH was replaced by DCOOH, the catalytic decomposition of DCOOH in H_2O with **2**(SO_4) afforded not only HD but also H_2 [54]. A significant deuterium kinetic isotope effect was observed in the catalytic decomposition of DCOOH because the rate-determining step is the β-deuterium elimination from the formate complex to produce the Rh^{III}-D complex (vide supra) [54]. The formation of H_2 suggests that the deuteride species ($[Rh^{III}(Cp^*)(D)(bpy)]^+$), formed by deuteride transfer from $DCOO^-$ to $[Rh^{III}(Cp^*)(bpy)(H_2O)]^{2+}$, undergoes rapid H/D exchange with H_2O to afford $[Rh^{III}(Cp^*)(H)(bpy)]^+$ that reacts with H^+ to produce H_2. When the decomposition of HCOOH was performed with **2**(SO_4) in D_2O, D_2 was formed as a major product (73 %) together with HD (24 %) and H_2 (3 %) [54]. In this case, hydride transfer from $HCOO^-$ to $[Rh^{III}(Cp^*)(bpy)(H_2O)]^{2+}$ occurs to afford $[Rh^{III}(Cp^*)(H)(bpy)]^+$ that undergoes H/D exchange with D^+ to produce $[Rh^{III}(Cp^*)(D)(bpy)]^+$ [54]. Then, the reaction of $[Rh^{III}(Cp^*)(D)(bpy)]^+$ with D^+ yields D_2 as the main product [54]. The unexchanged hydride complex $[Rh^{III}(Cp^*)(H)(bpy)]^+$ reacts with D^+ and a small amount of H^+ derived from HCOOH to yield HD and a small amount of H_2, respectively [54]. Thus, rapid

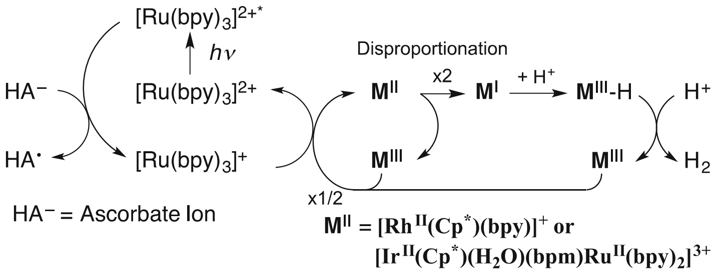

Scheme 11.3 Catalytic mechanism of hydrogen evolution with **2** or **3** as a proton reduction catalyst, ascorbate as an electron donor, and $[Ru(bpy)_3]^{2+}$ as a photocatalyst

H/D exchange between the hydride (or deuteride) species and proton (or deuteron) occurs as shown in Scheme 11.2, suggesting that the formal hydride species has a protic character.

The protic character of the hydride species was confirmed by formation of $[Rh^{I}(Cp^{*})(bpy)]$ by deprotonation from $[Rh^{III}(Cp^{*})(H)(bpy)]^{+}$ with a base (NaOH) [54]. Such a protic character of metal-hydride species was reported for the corresponding Ir complex with the same ligand as the Rh complex, i.e., $[Ir^{III}(Cp^{*})(H)(bpy)]^{+}$, which undergoes efficient H/D exchange with deuteron [55, 56]. DFT calculations showed that the positive charge of metal-hydride (M-H) (+0.571) was larger for $[Ir^{III}(Cp^{*})(H)(bpy)]^{+}$ as compared to the value for $[Rh^{III}(Cp^{*})(H)(bpy)]^{+}$ (+0.481) [54].

The Rh(III) complex (**2**(SO_4)) can also be used as a proton reduction catalyst in photocatalytic hydrogen evolution with ascorbate (HA^{-}) as an electron donor and $[Ru(bpy)_3]^{2+}$ as a photocatalyst [57]. The photocatalytic mechanism is shown in Scheme 11.3, where photoinduced electron transfer from HA^{-} to $[Ru(bpy)_3]^{2+*}$ (* denotes an excited state) occurs to produce $[Ru(bpy)_3]^{+}$, which reduces $[Rh^{III}(Cp^{*})(bpy)]^{2+}$ to $[Rh^{II}(Cp^{*})(bpy)]^{+}$, which was detected as a transient absorption band at 750 nm in Fig. 11.4a [57]. Disproportionation of $[Rh^{II}(Cp^{*})(bpy)]^{+}$ occurs to produce $Rh^{I}(Cp^{*})(bpy)$ and $[Rh^{II}(Cp^{*})(bpy)]^{+}$ as indicated by the second-order decay of absorbance at 750 nm due to $[Rh^{II}(Cp^{*})(bpy)]^{+}$ (see the second-order plot in inset of Fig. 11.4b) [57]. $Rh^{I}(Cp^{*})(bpy)$ is protonated to produce the hydride complex ($[Rh^{III}(Cp^{*})(H)(bpy)]^{+}$), which reacts with proton to produce H_2, accompanied by regeneration of $[Rh^{III}(Cp^{*})(bpy)]^{2+}$ [57]. In the same manner, when a heterodinuclear iridium–ruthenium complex $[Ir^{III}(Cp^{*})(H_2O)(bpm)Ru^{II}(bpy)_2](SO_4)_2$ (**3**$(SO_4)_2$, bpm = 2,2-bipyrimidine) was used in place of **2**(SO_4), photocatalytic H_2 evolution was confirmed to proceed via disproportionation of $[Ir^{II}(Cp^{*})(H_2O)(bpm)Ru^{II}(bpy)_2]^{3+}$. Thus, disproportionation of $[Rh^{II}(Cp^{*})(bpy)]^{+}$ or $[Ir^{II}(Cp^{*})(H_2O)(bpm)Ru^{II}(bpy)_2]^{3+}$ is the key step to convert one-electron process induced by one photon to the two-electron process for H_2 evolution (Scheme 11.3). This shows sharp contrast to the case of $[Co^{III}(CR)Cl_2]^{+}$, which is reduced by HA^{-} to produce the Co(II) complex, which is further reduced to the Co (I) complex via photoinduced electron transfer from $[Ru(bpy)_3]^{2+*}$ to the Co (II) complex (vide supra) [50].

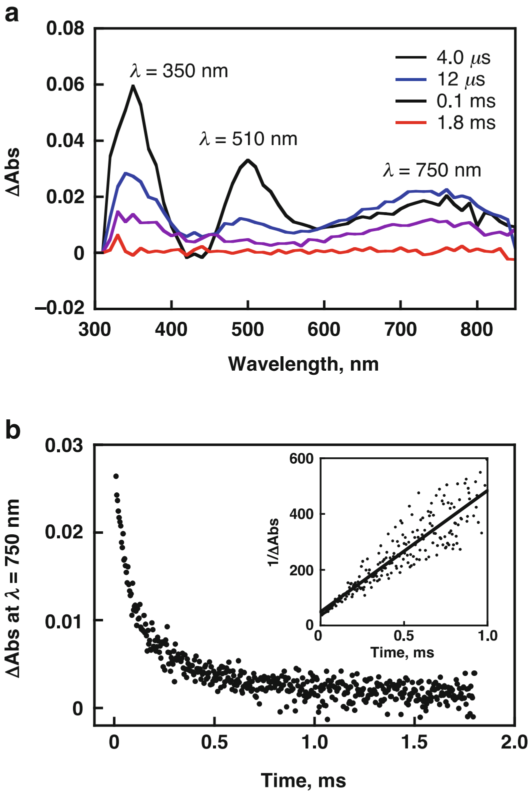

Fig. 11.4 (**a**) Transient absorption spectra of **2** (SO_4) (1.6×10^{-4} M) after laser excitation of $[Ru(bpy)_3]^{2+}$ (8.0×10^{-5} M) at $\lambda = 455$ nm in the presence of H_2A (0.8 M) and NaHA (0.3 M) in deaerated H_2O at pH 3.6 at 298 K. (**b**) Decay time profile of absorbance at $\lambda = 750$ nm due to $[Rh^{II}(Cp^*)(bpy)]^+$. *Inset*: Second-order plot (Reproduced from Ref. [57] by permission of John Wiley & Sons Ltd)

The same type of photocatalytic H_2 evolution with ascorbate and $[Ru(bpy)_3]^{2+}$ occurs using $[Rh^{III}(dmbpy)_2Cl_2]Cl$ (dmbpy = 4,4′-dimethyl-2,2′-bipyridine) as a proton reduction catalyst [58]. The catalytic reactivity of $[Rh^{III}(dmbpy)_2Cl_2]Cl$ was higher than that of $[Rh^{III}(Cp^*)(bpy)]^{2+}$ to afford high TON and TOF values (1,010 and 857 h^{-1}) at pH 4.0 [58]. The high catalytic activity may result from formation of colloidal rhodium nanoparticles during the photocatalytic reaction, which are known to promote the reduction of protons into H_2 [59]. This possibility was ruled out, because the addition of a large excess of mercury had no significant effect on the catalytic activity of $[Rh^{III}(dmbpy)_2Cl_2]Cl$. Mercury is known to form amalgam with colloidal metal or to adsorb to nanoparticular metal catalysts, and mercury poisoning has been reported for rhodium colloids [60].

11.2.2.1 Iridium Hydride Complexes

A heterodinuclear iridium–ruthenium complex $[Ir^{III}(Cp^*)(H_2O)(bpm)Ru^{II}(bpy)_2](SO_4)_2$ (**3**$(SO_4)_2$, bpm = 2,2-bipyrimidine) also acts as an efficient catalyst for H_2 evolution from HCOOH in an aqueous solution at 298 K [61]. The maximum TOF

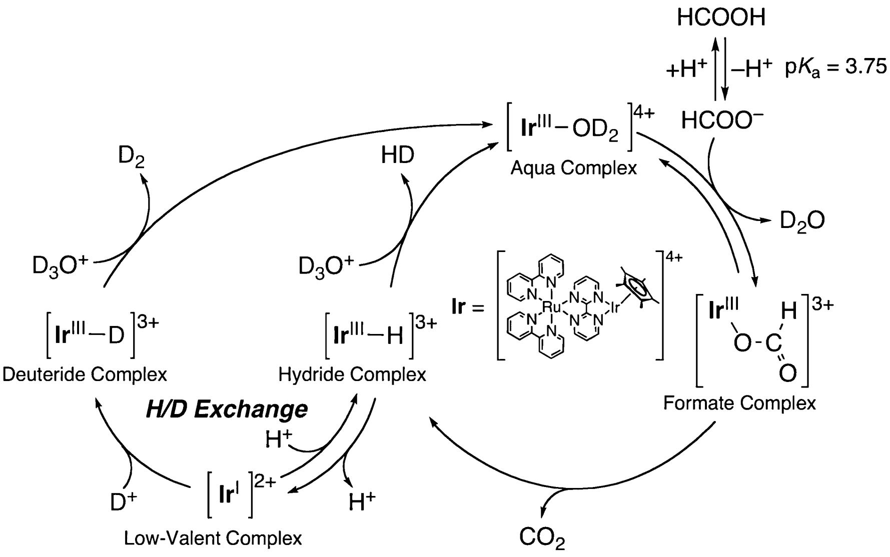

Scheme 11.4 Catalytic mechanism of decomposition of HCOOH by **3** in D_2O

value (426 h^{-1}) was obtained at pH 3.8 which agrees with the pK_a value of HCOOH [61]. The TOF value is much higher than that of $[Rh^{III}(Cp^*)(bpy)(H_2O)](SO_4)$ under the same experimental conditions (TOF = 27 h^{-1}) [61]. The catalytic mechanism is shown in Scheme 11.4, which is similar to the case of $[Rh^{III}(Cp^*)(bpy)(H_2O)](SO_4)$ in Scheme 11.2 [61]. The reaction of $\mathbf{3}^{4+}$ with $HCOO^-$ affords the formate complex ($[Ir^{III}(Cp^*)(O(CO)H)(bpm)Ru^{II}(bpy)_2]^{3+}$), followed by β-hydrogen elimination to give the Ir–hydride complex ($[Ir^{III}(Cp^*)(H)(bpm)Ru^{II}(bpy)_2]^{3+}$) which reacts with H^+ to produce H_2, accompanied by regeneration of $\mathbf{3}^{4+}$ [61]. Rapid H/D exchange between the hydride (or deuteride) species and proton (or deuteron) also occurs as the case of $\mathbf{2}^{2+}$ in Scheme 11.2 [61]. In Scheme 11.4, however, the rate-determining step in the overall hydrogen evolution reaction is not the β-hydrogen elimination step but the reaction of the hydride complex with H^+ to evolve H_2 at pH 3.8 [61]. The Arrhenius plots for TOF in D_2O (red circles) vs. H_2O (black circles) in Fig. 11.5 afforded $A_H/A_D = 3.1 \times 10^{-5}$, $E_a(D)-E_a(H) = 8.2$ kcal mol^{-1}, and an unusually large KIE value at 298 K (KIE = 40) [61]. Such values for the Arrhenius parameters $A_H/A_D << 1$ and $E_a(D)-E_a(H) > 1.2$ kcal mol^{-1} together with a large KIE value at 298 K (KIE > 9) are generally taken to unambiguously demonstrate the involvement of tunneling [62–65]. Because a protic character of metal-hydride species is more enhanced for the Ir–hydride complex as compared with the Rh-hydride complex, the reaction of the Ir–hydride complex with proton becomes the rate-determining step.

The catalytic activity for hydrogen evolution from formic acid was further enhanced by using a C^N cyclometalated organoiridium complex, $[Ir^{III}(Cp^*)\{4\text{-}(1H\text{-pyrazol-1-yl-}\kappa N^2)\text{benzoic acid-}\kappa C^3\}(H_2O)]_2SO_4$ ($[\mathbf{4}]_2 \bullet SO_4$, Fig. 11.6), as a

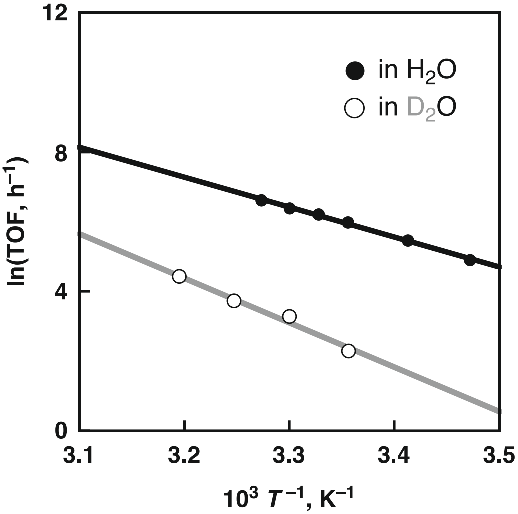

Fig. 11.5 Arrhenius plots of TOF for the decomposition of HCOOH/HCOONa (3.1 M) catalyzed by **3**$(SO_4)_2$ (0.3 mM) in deaerated H_2O (*closed circles*) or D_2O (*open circles*) at pH 3.8 or pD 3.8, respectively (Reprinted with the permission from Ref. [61]. Copyright 2010 American Chemical Society)

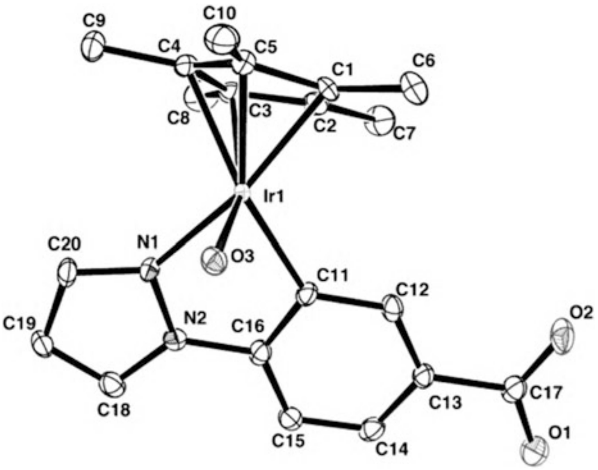

Fig. 11.6 ORTEP drawing of **4**. Hydrogen atoms are omitted for clarity (Reprinted with the permission from Ref. [68]. Copyright 2012 American Chemical Society)

catalyst with TOF value over 2,000 h^{-1} at 298 K (Fig. 11.7) [66]. The catalytic mechanism is shown in Scheme 11.5 [66].

As pH was increased, the Ir(III) complex [**Ir**$^{\mathbf{A}}$–H_2O]$^+$ released protons from the carboxy group and the aqua ligand to form the corresponding benzoate complex [**Ir**$^{\mathbf{B}}$–H_2O]^0 and the hydroxo complex [**Ir**$^{\mathbf{B}}$–OH]$^-$, respectively (Scheme 11.6). The pK_a values of [**Ir**$^{\mathbf{A}}$–H_2O]$^+$ and [**Ir**$^{\mathbf{B}}$–H_2O]^0 were determined from the spectral titration to be p$K_{a1} = 4.0$ and p$K_{a2} = 9.5$, respectively [66]. The saturation behavior of TOF of hydrogen evolution with increasing concentration of [HCOOH] + [HCOOK] at pH 2.8 (Fig. 11.7) indicates that hydrogen is produced via the formate complex of [**Ir**$^{\mathbf{A}}$–H_2O]$^+$, followed by β-elimination to produce the hydride

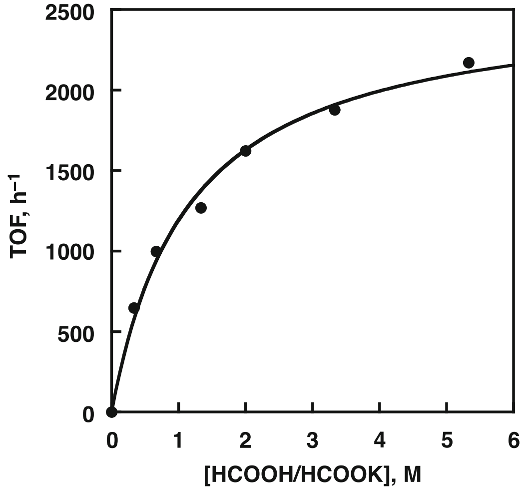

Fig. 11.7 Plot of TOF vs. concentration of HCOOH and HCOOK mixture (HCOOH/HCOOK), i.e., [HCOOH] + [HCOOK] in the decomposition of HCOOH/HCOOK catalyzed by [**Ir**$^{\mathbf{A}}$–H_2O]$^+$ (0.20 mM) in deaerated H_2O at pH 2.8 at 298 K (Reproduced from Ref. [66] by permission of The Royal Society of Chemistry)

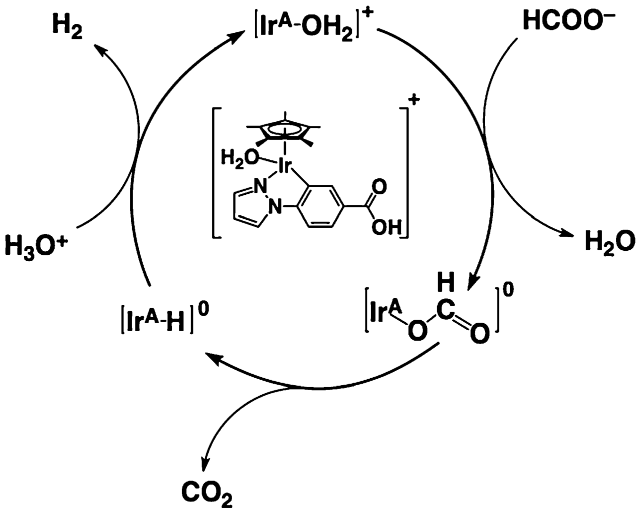

Scheme 11.5 Catalytic mechanism of H_2 evolution and decomposition of $HCOO^-$ with **4** in H_2O

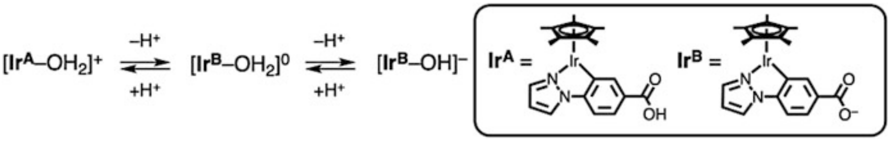

Scheme 11.6 Acid–base equilibria of iridium aqua complexes

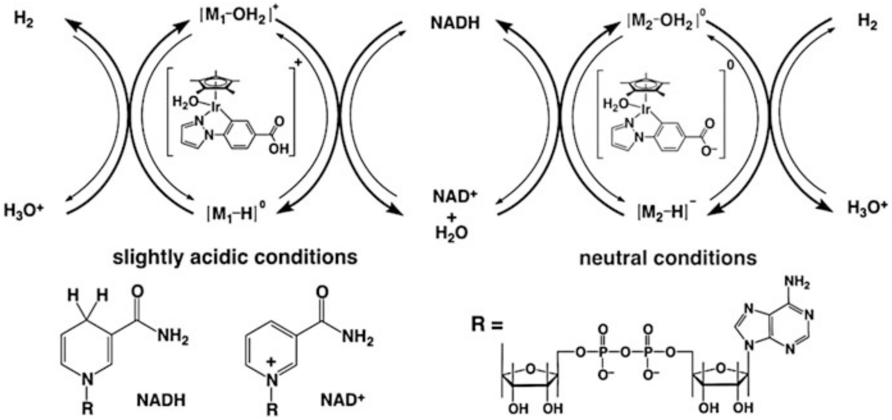

Scheme 11.7 Catalytic mechanism of interconversion between H_2 and NADH with **4** in H_2O

complex, which reacts with proton to produce H_2 (Scheme 11.6) [66]. The activation energy was determined to be 18.9 kcal mol^{-1}, which is much smaller than the activation energy of the decomposition of formic acid without catalysts (78 kcal mol^{-1}) [67].

The C^N cyclometalated organoiridium complex $[\mathbf{Ir^A}–H_2O]^+$ can also act as an efficient catalyst for hydrogen evolution from NADH (dihydronicotinamide adenine dinucleotide), which is a natural electron and proton source in respiration and CO_2 fixation [68], in water at pH 4.1 [69]. NADH has been frequently used as an electron and proton source in photocatalytic hydrogen evolution with a photocatalyst and a proton reduction catalyst [70–73]. Under acidic conditions, NADH can reduce thermally proton to produce H_2 and NAD^+ by the catalysis of $[\mathbf{Ir^A}–H_2O]^+$ (Eq. **11.6**). The catalytic cycle is shown in Scheme 11.7 [69]. Under acidic

$$\mathrm{NADH} + \mathrm{H}^+ \xrightarrow[{[\mathbf{Ir^A} - \mathrm{H_2O}]^+}]{} \mathrm{NAD}^+ + \mathrm{H_2} \qquad (11.6)$$

conditions, hydride transfer from NADH to $[\mathbf{Ir^A}–H_2O]^+$ occurs to produce NAD^+ and the Ir(III)-hydride complex $[\mathbf{Ir^A}–H]^0$, which reacts with H_3O^+ to produce H_2, accompanied by regeneration of $[\mathbf{Ir^A}–H_2O]^+$ [69]. Under basic conditions, however, the catalytic cycle was reversed, when H_2 can reduce the deprotonated carboxylate form $[\mathbf{Ir^B}–H_2O]^0$ to produce the Ir(III)-hydride complex, which reduces NAD^+ to NADH, accompanied by regeneration of the deprotonated form of $[\mathbf{Ir^B}–H_2O]^0$ [69]. Thus, interconversion between NADH and H_2 at ambient pressure and temperature can be efficiently catalyzed by $[\mathbf{Ir^A}–H_2O]^+$ and $[\mathbf{Ir^B}–H_2O]^0$ depending on pH.

According to Scheme 11.6, the Ir(III) complex $[\mathbf{Ir^A}–H_2O]^+$ is converted to the hydroxo complex $[\mathbf{Ir^B}–OH]^-$ at pH 13.6. When ethanol was added to an aqueous solution of $[\mathbf{Ir^B}–OH]^-$ at pH 13.6, hydride transfer from ethanol to $[\mathbf{Ir^B}–OH]^-$

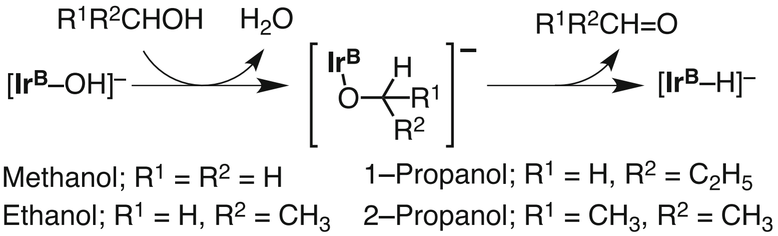

Scheme 11.8 Dehydrogenation reaction of alcohols by $[\mathrm{Ir^B}\text{–}\mathrm{OH}]^-$ in H_2O

occurred to produce acetaldehyde and the hydride complex $[\mathbf{Ir^B}\text{–}\mathrm{H}]^-$ [74]. When CD_3CD_2OH in place of CH_3CH_2OH was added to an aqueous solution of $[\mathbf{Ir^B}\text{–}\mathrm{OH}]^-$, a kinetic deuterium isotope effect (KIE) for the formation of $[\mathbf{Ir^B}\text{–}\mathrm{D}]^-$ was observed to be $k_H/k_D = 2.1$ [74]. The observation of KIE indicates that the reaction of ethanol with $[\mathbf{Ir^B}\text{–}\mathrm{OH}]^-$ involves the C–H bond cleavage. Thus, the β-hydrogen elimination of the ethoxy complex which is produced by the replacement of a hydroxy (OH) ligand of $[\mathbf{Ir^B}\text{–}\mathrm{OH}]^-$ by a ethoxy (CH_3CH_2O) ligand, may be the rate-determining step for formation of the hydride complex $[\mathbf{Ir^B}\text{–}\mathrm{H}]^-$ (Scheme 11.8). Other alcohols can also reduce $[\mathbf{Ir^B}\text{–}\mathrm{OH}]^-$ to produce the hydride complex $[\mathbf{Ir^B}\text{–}\mathrm{H}]^-$ [74].

The hydride complex $[\mathbf{Ir^B}\text{–}\mathrm{H}]^-$ is stable at pH 14. When pH was decreased to 0.8 by adding H_2SO_4, however, the hydride complex $[\mathbf{Ir^B}\text{–}\mathrm{H}]^-$ was converted to an aqua complex $[\mathbf{Ir^A}\text{–}\mathrm{H_2O}]^+$ as shown by Fig. 11.8a, accompanied by evolution of hydrogen (H_2) [74]. The conversion between the hydride complex $[\mathbf{Ir^B}\text{–}\mathrm{H}]^-$ and the aqua complex $[\mathbf{Ir^A}\text{–}\mathrm{H_2O}]^+$ accompanied by H_2 evolution was repeated by alternate change in pH between 12 and 2 in the presence of excess amount of ethanol as shown in Fig. 11.8b (Scheme 11.9) [74]. Without changing pH, however, no catalytic H_2 evolution from ethanol occurred with $[\mathbf{Ir^A}\text{–}\mathrm{OH}]^0$ [74].

Photoirradiation of the hydride complex $[\mathbf{Ir^B}\text{–}\mathrm{H}]^-$ resulted in the conversion to the [C,C] cyclometalated complex $[\mathbf{Ir^C}\text{–}\mathrm{H}]^-$ (Scheme 11.10) [74]. In contrast to the [C,N] cyclometalated Ir–hydride complex $[\mathbf{Ir^B}\text{–}\mathrm{H}]^-$, the [C,C] cyclometalated Ir–hydride complex $[\mathbf{Ir^C}\text{–}\mathrm{H}]^-$ can react with water to produce H_2 under basic conditions as shown in Fig. 11.9. The turnover number (TON) of H_2 evolution from isopropanol with $[\mathbf{Ir^C}\text{–}\mathrm{H}]^-$ (Eq. 11.7) increases linearly with time to reach 3.3 (2.5 h), whereas $[\mathbf{Ir^B}\text{–}\mathrm{H}]^-$ has no catalytic reactivity even at elevated temperature at 323 K (Fig. 11.9). TON for H_2 evolution from isopropanol with $[\mathbf{Ir^C}\text{–}\mathrm{H}]^-$ increases with increasing temperature to be 26 (1.0 h) at 353 K (Fig. 11.9) [74]. The enhanced catalytic activity of $[\mathbf{Ir^C}\text{–}\mathrm{H}]^-$ results from the electronic donating effect of phenylpyrazole ligand on the metal center with a [C,C] cyclometalated iridium as indicated by the upfield shift of a hydride signal bonded to $\mathrm{Ir^{III}}$ center ($\delta = -17.48$) as compared with that of $[\mathbf{Ir^B}\text{–}\mathrm{H}]^-$ ($\delta = -14.34$) [74]:

$$\underset{[\mathbf{Ir^C} - \mathrm{H}]^-}{(\mathrm{CH_3})_2\mathrm{CHOH} \rightarrow (\mathrm{CH_3})_2\mathrm{CO} + \mathrm{H_2}} \tag{11.7}$$

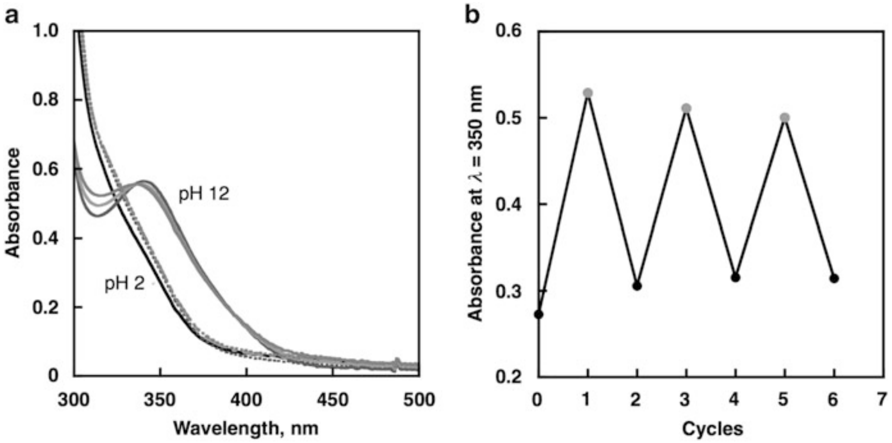

Fig. 11.8 (**a**) UV-vis absorption spectral change of an aqueous solution of [**Ir**$^{\mathbf{B}}$–OH]$^-$ (0.12 mM) and ethanol (82 mM) by alternate change in pH. (**b**) Changes of absorbance at $\lambda = 350$ nm due to the formation of a hydride complex [**Ir**$^{\mathbf{B}}$–H]$^-$ in the reaction of [**Ir**$^{\mathbf{B}}$–OH]$^-$ (0.12 mM) with ethanol (82 mM) in water (pH 11.8–12.2) and due to the hydrogen evolution in the reaction of the hydride complex [**Ir**$^{\mathbf{B}}$–H]$^-$ with proton in water at 298 K (pH 2.0–3.3) by adding an aqueous solution of H_2SO_4 (5.0 M) or NaOH (5.0 M) (Reprinted with the permission from Ref. [74]. Copyright 2012 American Chemical Society)

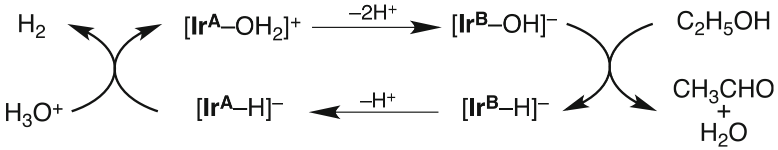

Scheme 11.9 Catalytic mechanism of H_2 evolution from ethanol with $[Ir^A–H_2O]^+$ in H_2O

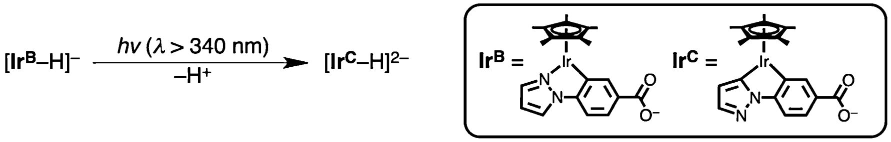

Scheme 11.10 Conversion from a [C,N] to [C,C] cyclometalated Ir complex under photoirradiation

11.2.2.2 Ruthenium Hydride Complexes

The catalytic activity of hydrogen evolution from alcohols has been reported to be remarkably enhanced by using ruthenium complexes containing pincer-type ligands [75]. Catalytic hydrogen evolution occurred in methanol containing KOH (8.0 M) with $[RuHCl(CO)(HN(C_2H_4P^iPr_2)_2)]$ (**5**), which exhibited high activities

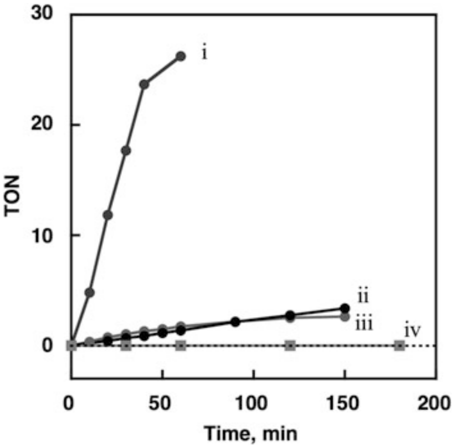

Fig. 11.9 Time course of H_2 evolution from 2-propanol (4.3 M) catalyzed by 5 (55 μM) in water (pH 11.9) at 353 K *i*) and 323 K (*ii*) and that from ethanol (5.7 M) catalyzed by $[\mathbf{Ir}^C\text{–H}]^-$ (55 μM) in water (pH 11.9) at 323 K (*iii*). Time course of H_2 evolution from 2-propanol (4.3 M) catalyzed by $[\mathbf{Ir}^B\text{–H}]^-$ (55 μM) in water (pH 11.9) at 323 K (*iv*) (Reprinted with the permission from Ref. [74]. Copyright 2012 American Chemical Society)

up to $TOF = 4{,}700\ h^{-1}$ and $TON = 350{,}000$ at 368 K [75]. Under catalytic conditions, both formate and carbonate ions were observed as traces of the reaction mixtures, indicating that the formate is an intermediate in this dehydrogenation sequence and that CO_2 is trapped as carbonate [75]. The overall stoichiometry of the hydrogen evolution from methanol with NaOH is given by Eq. 11.8. The Ru-hydride species were observed in solution under catalytic conditions [75]:

$$CH_3OH + 2NaOH \xrightarrow[\mathbf{5}]{} 3H_2 + Na_2CO_3 \tag{11.8}$$

Base-free hydrogen evolution from methanol without formation of CO has recently been achieved by using the ruthenium-based PNP pincer complex (**6**: Ru-MACHO-BH) in Eq. 11.9 [76]. The combination of Ru-MACHO-BH (**6**) with $Ru(H)_2(dppm)_2$ (**7**) further enhanced the catalytic activity for hydrogen evolution from neutral methanol [76]. A long-term experiment gave a 26 % yield of H_2 (relative to H_2O) and a $TON > 4{,}200$ [76]. In this case full conversion of all "available" hydrogen atoms in methanol to H_2 has been achieved by synergetic homogeneous catalysis of **6** and **7** [76]:

$$CH_3OH + H_2O \xrightarrow[\mathbf{6},\qquad\qquad \mathbf{7}]{} 3H_2 + CO_2 \tag{11.9}$$

Hydrogen is also produced by the electrocatalytic reduction of protons with a Ru (II) complex $[Ru^{II}(tpy)(bpy)(S)]^{2+}$ (tpy = 2,2′:6′,2″-terpyridine, bpy = 2,2-′-bipyridine, S = solvent) in acetonitrile (MeCN) [77]. The Ru(II)-hydride complex

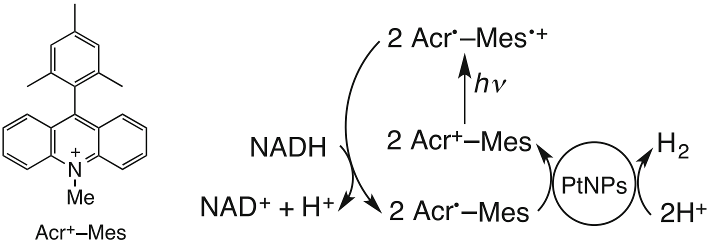

Scheme 11.11 Chemical structure of Acr$^+$–Mes and overall photocatalytic cycle for H_2 evolution

$[Ru^{II}(tpy)(bpy)(H)]^+$ is produced by the reaction of the ligand-based two-electron-reduced species $[Ru^{II}(tpy^{\bullet -})(bpy^{\bullet -})(MeCN)]^0$ with water (Eq. 11.10) [77]:

$$[Ru^{II}(tpy^-)(bpy^-)(MeCN)]^0 + H_2O \rightarrow [Ru^{II}(tpy)(bpy)(H)]^+ + OH^- \quad (11.10)$$

Further reduction of the hydride to $[Ru^{II}(tpy^{\bullet -})(bpy)(H)]^0$ at -1.41 V (vs. NHE) is proposed to trigger the catalytic water reduction via formation of the dihydrogen–dihydride complex $[Ru^{II}(tpy)(bpy)(H_2)]^+$ (Eqs. 11.11, 11.12, and 11.13) [77]. However, this intermediate has yet to be detected. In the presence of an acid,

$$[Ru^{II}(tpy^-)(bpy)(H)]^0 + H_2O \rightarrow [Ru^{II}(tpy^-)(bpy)(H_2)]^+ + OH^- \quad (11.11)$$

$$[Ru^{II}(tpy^-)(bpy)(H_2)]^+ + e^- \rightarrow [Ru^{II}(tpy^-)(bpy^-)(H_2)]^0 \quad (11.12)$$

$$[Ru^{II}(tpy^-)(bpy^-)(H_2)]^0 + MeCN \rightarrow H_2 + [Ru^{II}(tpy^-)(bpy^-)(MeCN)]^0 \quad (11.13)$$

$[Ru^{II}(tpy)(bpy)(H)]^+$ can react with H^+ to produce H_2 [77]. Many other metal hydrides are known to catalyze electrochemical reduction of protons to H_2 [78–83].

11.2.2.3 Proton-Coupled Electron Transfer to Metal Nanoparticles

Pt nanoparticles (PtNPs) act as the best catalyst for catalytic reduction of protons to H_2 [43]. Photocatalytic H_2 evolution occurred efficiently using NADH as a sacrificial electron donor, 9-mesityl-10-methylacridinium ion (Acr$^+$–Mes) [84] as an organic photocatalyst, and PtNPS as a proton reduction catalyst (Scheme 11.11) [85]. Photoexcitation of Acr$^+$–Mes resulted in intramolecular electron transfer from the Mes moiety to the singlet excited sate of the Acr$^+$ moiety to produce the electron-transfer state (Acr$^\bullet$–Mes$^{\bullet +}$) [84, 86–88]. NADH is oxidized by the Mes$^{\bullet +}$ moiety of Acr$^\bullet$–Mes$^{\bullet +}$ to produce two equivalents of Acr$^\bullet$–Mes. Electron transfer from Acr$^\bullet$–Mes to PtNPs with protons resulted in H_2 evolution [85].

The kinetics and mechanism of the PtNP-catalyzed hydrogen evolution by an Acr$^\bullet$–Mes were studied by simultaneous determination of the rate of hydrogen

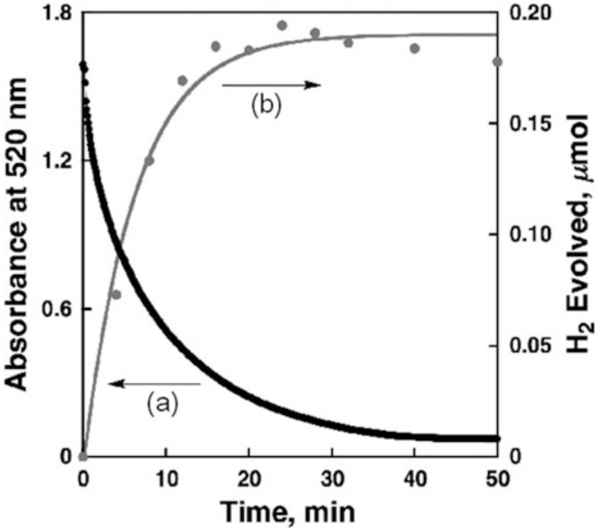

Fig. 11.10 (a) Time profile of electron transfer from Acr•–Mes to spherical PtNPs with the diameter of 4.5 nm (0.1 μg), monitored by decrease in absorbance at 520 nm due to Acr•–Mes in a (pH 5.0, 50 mM) CH_3COOH/CH_3COONa buffer and MeCN [1:1 (v/v)] mixed solution. (b) Time profile of H_2 evolution (Reproduced from Ref. [85] by permission of John Wiley & Sons Ltd)

evolution and the rate of electron transfer from Acr•–Mes to PtNPs [85]. The rate of H_2 evolution in a (pH 5.0, 50 mM) CH_3COOH/CH_3COONa buffer and MeCN [1:1 (v/v)] mixed solution is virtually the same as the rate of electron transfer from Acr•–Mes to PtNPs, which was monitored by decrease in absorbance at 520 nm due to Acr•–Mes as shown in Fig. 11.9 [85]. This indicates that electron transfer from Acr•–Mes to PtNPs is the rate-determining step for the catalytic H_2 evolution. The rate constant of electron transfer from Acr•–Mes to PtNPs (k_{et}) is proportional to proton concentration (Fig. 11.10) [85]. When CH_3COOH/CH_3COONa buffer (pH 4.5, 50 mM) in H_2O was replaced by CH_3COOD/CH_3COONa in D_2O, an inverse kinetic isotope effect (KIE = 0.68) was observed in electron transfer from Acr•–Mes to PtNPs [85]. Such an inverse kinetic isotope effect results from the difference in the zero-point energy for Pt–H (Pt–D) bond at the transition state as compared with that before electron transfer when the interaction between Pt and H^+ (or D^+) is much smaller as shown in Fig. 11.11 [85]. This indicates that proton-coupled electron transfer (PCET) from Acr•–Mes to PtNPs producing a Pt–H bond is the rate-determining step (r.d.s.) in the catalytic hydrogen evolution. The inverse KIE (0.68) in Fig. 11.12 shows sharp contrast to the large KIE (40) observed for the hydrogen evolution from formic acid, catalyzed by an Ir–hydride complex ($[Ir^{III}(Cp^*)(H)(bpm)Ru^{II}(bpy)_2]^{3+}$) when the heterolytic Ir–H bond cleavage by proton is the rate-determining step in Scheme 11.4 (vide supra) [61]. Based on the results in Figs. 11.10 and 11.12, the PtNP-catalyzed H_2 evolution mechanism was proposed as shown in Scheme 11.12 [85]. PCET from Acr•–Mes to PtNPs produces the Pt–H bond, followed by rapid elimination of H_2 from two Pt–H bonds.

When Acr^+–Mes was replaced by 2-phenyl-4-(1-naphthyl)quinolinium ion ($QuPh^+$–NA) [89], photocatalytic H_2 evolution also occurred efficiently with NADH and PtNPs (Scheme 11.12) [90]. However, the rate constant of electron transfer from QuPh•–NA to PtNPs was invariant with pH [90], in contrast to the

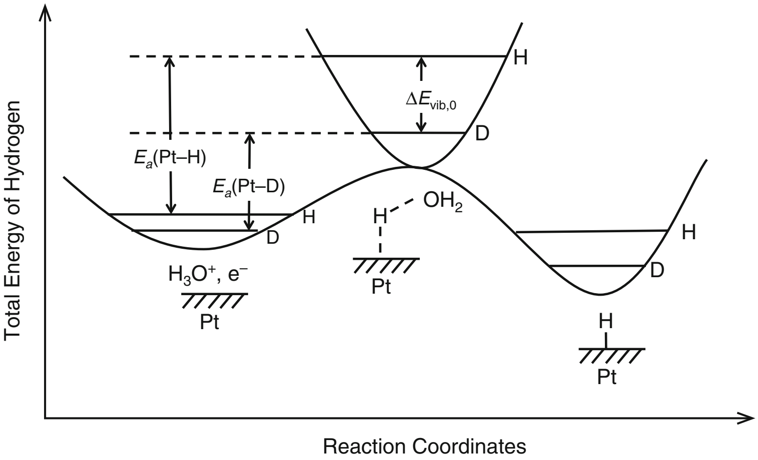

Fig. 11.11 Illustration of the PCET pathway to produce the Pt–H or Pt–D bond

Fig. 11.12 Dependence of k_{et} on [H^+] or [D^+] for electron transfer from Acr$^•$–Mes to spherical PtNPs with the diameter of 4.5 nm in H_2O/MeCN [1:1 (v/v)] containing CH_3COOH/CH_3COONa buffer (50 mM) or in D_2O/MeCN [1:1 (v/v)] containing CH_3COOD/CH_3COONa buffer (50 mM) at 298 K (Reproduced from Ref. [85] by permission of John Wiley & Sons Ltd)

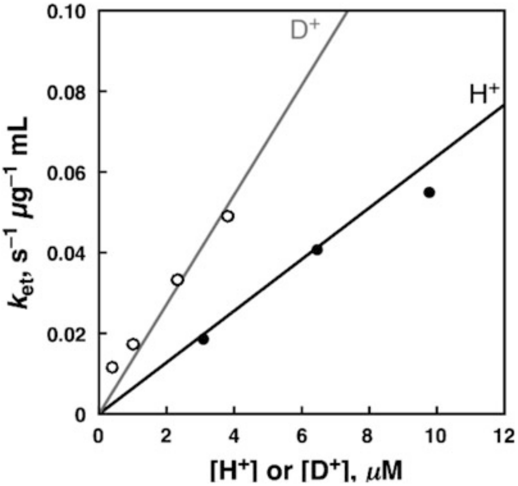

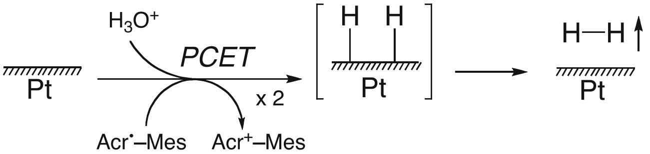

Scheme 11.12 Mechanism of H_2 evolution on Pt surfaces

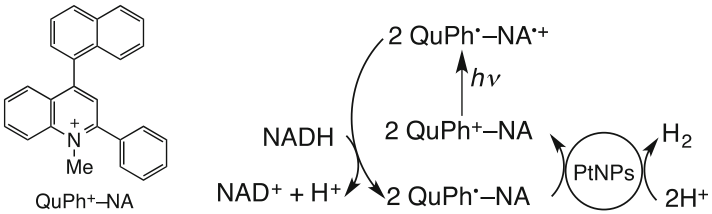

Scheme 11.13 Chemical structure of QuPh$^+$–NA and overall photocatalytic cycle for H_2 evolution

case of PCET from Acr$^•$–Mes to PtNPs in which the rate constant was proportional to proton concentration (Fig. 11.10) [85]. Thus, electron transfer from QuPh$^•$–NA to MNPs occurs without assistance of proton because of the much stronger reducing ability of QuPh$^•$–NA as compared with Acr$^•$–Mes judging from the significantly more negative oxidation potential of QuPh$^•$–NA ($E_{ox} = -0.90$ V vs. SCE) [89] than that of Acr$^•$–Mes ($E_{ox} = -0.57$ V vs. SCE) [84]. Because the rate of hydrogen evolution was much slower than the rate of electron transfer from QuPh$^•$–NA to MNPs and the hydrogen evolution was also pH independent at pH < 10, the rate-determining step of the catalytic H_2 evolution may be elimination of hydrogen from two Pt–H bonds [90]. Thus, the rate-determining step for the catalytic H_2 evolution is changed depending on the reducing ability of one-electron reductants (Scheme 11.13).

11.2.2.4 Kinetics and Mechanisms of Catalytic CO_2 Reduction

The catalytic reduction of CO_2 by H_2 has attracted significant interest because catalytic transformation of CO_2 would be promising for the production of fuels as liquid hydrogen sources and value-added chemicals [91–96]. However, the reactions involving CO_2 are commonly carried out at high pressure [97–106], which may not be economically suitable and also poses safety concerns. In order to improve the catalytic activity for the CO_2 reduction, it is of primary importance to elucidate the catalytic mechanism.

Kinetics and mechanism of the catalytic reduction of CO_2 by H_2 to produce formic acid (HCOOH) were reported by using $[Ir^{III}(Cp^*)(L)(H_2O)](SO_4)$ and $[Ru^{II}(\eta^6\text{-}C_6Me_6)(L)(H_2O)](SO_4)$ (L = bpy or 4,4′-OMe-bpy) as catalysts in water [107]. The rates of the catalytic reduction of CO_2 by H_2 with $[Ir^{III}(Cp^*)(L)(H_2O)](SO_4)$ under acidic conditions in H_2O are affected by the pressure of H_2 and CO_2. Turnover number (TON) of the catalytic reduction of CO_2 (2.5 MPa) by H_2 with $[Ir^{III}(Cp^*)(L)](SO_4)$ increased with increasing H_2 pressure at pH 3.0 at 40 °C to reach a constant value (Fig. 11.13a), whereas TON was proportional to CO_2 pressure at 5.5 MPa of H_2 (Fig. 11.13b). The reactions of $[Ir^{III}(Cp^*)(L)$

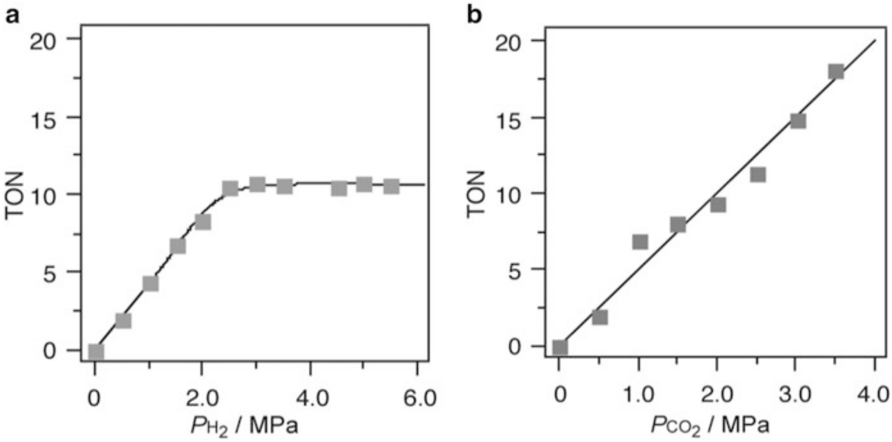

Fig. 11.13 (**a**) Dependence of TONs at 0.5 h on H_2 pressure for the reduction of CO_2 (2.5 MPa) by H_2 catalyzed by **6**(SO_4) (20 μmol) at pH 3.0 in a citrate buffer solution (20 cm^3) at 40 °C. (**b**) Dependence TONs at 0.5 h on CO_2 pressure for the reduction of CO_2 by H_2 (5.5 MPa) catalyzed by the **6**(SO_4) (20 μmol) at pH 3.0 in a citrate buffer solution (20 cm^3) at 40 °C (Reproduced from Ref. [107] by permission of The Royal Society of Chemistry)

(H_2O)](SO_4) with H_2 at pH 3.0 in a citrate buffer solution provide the Ir(III)–hydride complexes [Ir^{III}(Cp^*)(L)(H)]$_2$(SO_4), which were detected by the ESI-mass spectra and ^{1}H NMR spectra. Because TON of the catalytic reduction of CO_2 by H_2 was proportional to CO_2 pressure, the rate-determining step may be the reaction of the Ir(III)–hydride complex with CO_2 to produce the formate complex as shown in Scheme 11.14. In such a case, the rate of formation of HCOOH in the catalytic reduction of CO_2 by H_2 with [Ir^{III}(Cp^*)(L)(H_2O)](SO_4) is given by Eq. 11.14,

$$\mathrm{d[HCOOH]/d}t = k_1k_2[[\mathrm{Ir{-}OH_2}]^{2+}]P_{\mathrm{H2}}P_{\mathrm{CO2}}/(k_{-1} + k_1P_{\mathrm{H2}}) \tag{11.14}$$

where k_1 is the rate constant of the reaction of the aqua complexes [Ir^{III}(Cp^*)(L)(H_2O)]$^{2+}$ with H_2, k_{-1} is the rate constant of the back reaction, k_2 is the rate constant of the reaction of the hydride complex [Ir^{III}(Cp^*(L)(H))]$^+$ with CO_2, and [[Ir–OH_2]$^{2+}$]$_0$ is the initial concentration of [Ir^{III}(Cp^*)(L)(H_2O)]$^{2+}$ [107]. Under the conditions such that $k_1P_{H2} >> k_{-1}$, the rate of formation of HCOOH becomes constant at large H_2 pressure as observed in Fig. 11.13a [107].

When [Ir^{III}(Cp^*)(L)(H_2O)](SO_4) was replaced by [Ru^{II}(η^6-C_6Me_6)(L)(H_2O)](SO_4), TON was proportional to H_2 pressure at 40 °C (Fig. 11.14a), whereas TON exhibited a saturation behavior with increasing CO_2 pressure (Fig. 11.14b) [107]. In such a case, the rate-determining step was changed from the reaction of the Ir(III)–hydride complex with CO_2 to produce the formate complex to the reaction of the Ru(III)–aqua complex with H_2 to produce the Ru(III)–hydride complex (Scheme 11.15) [107]. The rate of formation of HCOOH is given by Eq. 11.15,

Scheme 11.14 Catalytic mechanism of CO_2 reduction by H_2 with $[Ir^{III}(Cp^*)(L)(H_2O)](SO_4)$ to form HCOOH in H_2O

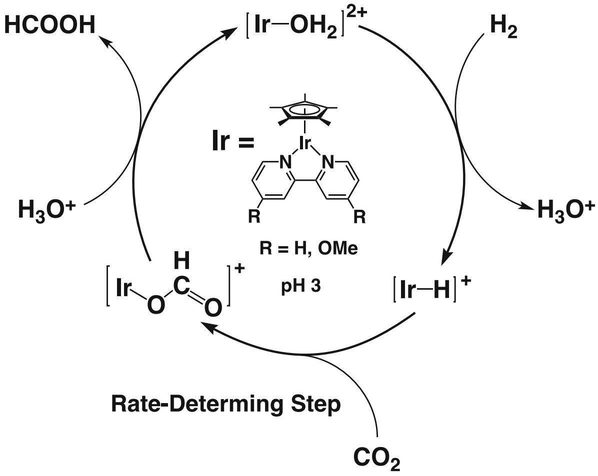

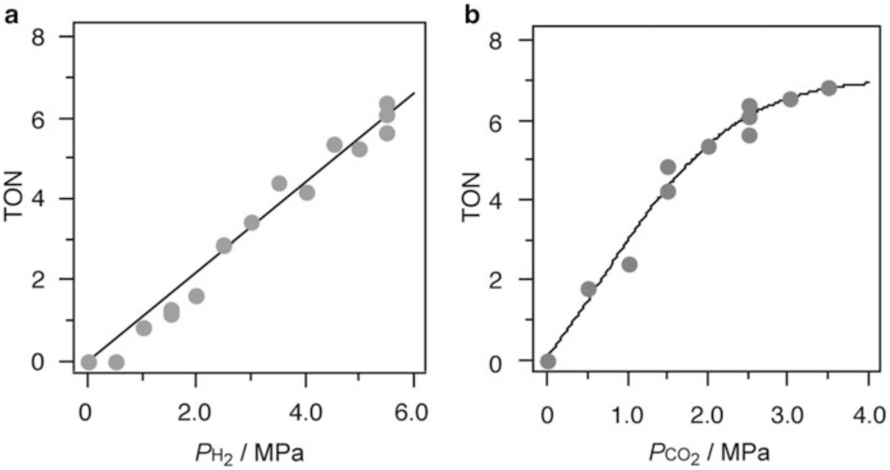

Fig. 11.14 (**a**) Dependence of TONs at 3 h on H_2 pressure for the reduction of CO_2 (2.5 MPa) by H_2 catalyzed by **2**(SO_4) (20 μmol) at pH 3.0 in a citrate buffer solution (20 cm^3) at 40 °C. (**b**) Dependence of TONs at 3 h on CO_2 pressure for the reduction of CO_2 by H_2 (5.5 MPa) catalyzed by **2**(SO_4) (20 μmol) at pH 3.0 in a citrate buffer solution (20 cm^3) at 40 °C (Reproduced from Ref. [107] by permission of The Royal Society of Chemistry)

which indicates that the rate becomes constant at large CO_2 pressure as observed in Fig. 11.14b [107]. The Ru(III)–hydride complex, which was prepared independently by the reaction of the Ru(III)–aqua complex with $NaBH_4$, reacted with CO_2 to produce the formate complex, which was detected by ESI-mass and ^1H NMR spectra [108, 109]:

$$\mathrm{d[HCOOH]}/\mathrm{d}t = k_1k_2[[\mathrm{Ru{-}OH_2}]^{2+}]P_{\mathrm{H2}}P_{\mathrm{CO2}}/(k_{-1}+k_2P_{\mathrm{CO2}}) \tag{11.15}$$

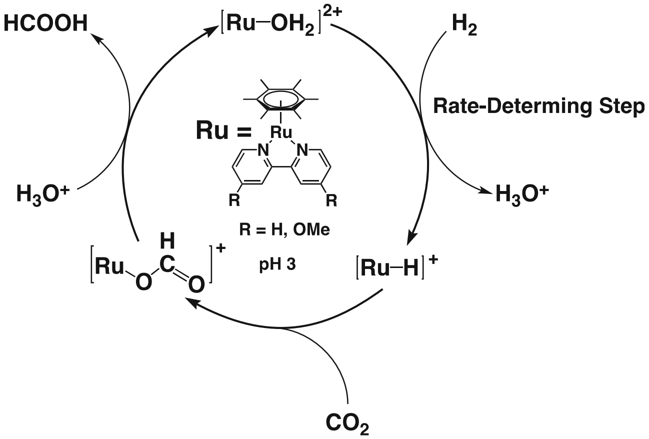

Scheme 11.15 Catalytic mechanism of CO_2 reduction by H_2 with $[Ru^{II}(\eta^6\text{-}C_6Me_6)(L)(H_2O)](SO_4)$ to form HCOOH in H_2O

The change in the rate-determining step in the catalytic reduction of CO_2 by H_2 between the Ir and Ru complexes results from the stronger Ir–H bond as compared with the Ru–H bond as indicated by the higher Ir–H stretching frequency (2,056 cm^{-1}) than the Ru–H stretching frequency (1,899 cm^{-1}) [107]. The stronger Ir–H bond facilitates the formation of the Ir–H bond, but decelerates the Ir–H bond cleavage by CO_2, which becomes the rate-determining step in the Ir complex-catalyzed CO_2 reduction by H_2. Conversely the weaker Ru–H bond facilitates the Ru–H bond cleavage by CO_2 but decelerates the formation of the Ru–H bond, which becomes the rate-determining step. The initial TOF for the catalytic reduction of CO_2 by H_2 with $[Ir^{III}(Cp^*)(L)(H_2O)](SO_4)$ was improved from 1 h^{-1} (L = bpy) to 27 h^{-1} (L = 4,4′-OMe-bpy) [107]. Thus, the more electron-rich Ir–H complex exhibits the higher catalytic reactivity. The X-ray crystal structures of the Ir–H and Ru–H complexes are shown in Fig. 11.15 [55, 109]. In both cases, the hydride complexes adopt a distorted octahedral coordination which has a terminal hydride ligand.

The catalytic activity for the reduction of CO_2 to HCOOH was enhanced by using a C^N cyclometalated organoiridium complex ($[Ir^{III}(Cp^*)\{4\text{-}(1H\text{-pyrazol-1-yl-}\kappa N^2)\text{benzoic acid-}\kappa C^3\}(H_2O)]_2SO_4$ ($[\mathbf{Ir^A}-H_2O]^+$)), which was employed for the catalytic decomposition of HCOOH to H_2 under acidic conditions in Fig. 11.7 (vide supra) [66]. At pH 7.5, the carboxylic acid is deprotonated to produce the more electron-rich Ir complex ($[\mathbf{Ir^B}-H_2O]^0$) when the direction of the reaction was reversed and the catalytic reduction of CO_2 by H_2 with $[\mathbf{Ir^B}-H_2O]^0$ occurred to produce formate at ambient pressure and temperature as shown in Fig. 11.16, where TON increased linearly with time to exceed over 100 [66]. Turnover frequency (TOF) increased with decrease in pH to afford the highest value at pH 8.8 and decreased with further increase in pH to reach zero at pH 10.4 [66]. The pH dependence of TOF is similar to pH dependence of the amount ratios of $[\mathbf{Ir^B}-H_2O]^0$

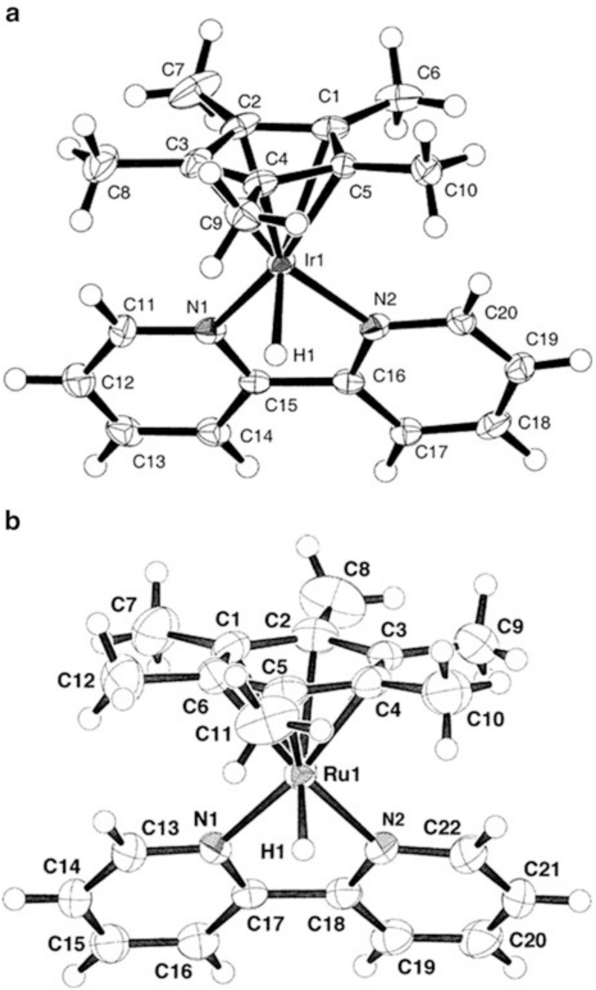

Fig. 11.15 ORTEP drawings of (**a**) $[Ir^{III}(Cp^{*})(bpy)(H)](PF_6)$ [109] and (**b**) $[Ru^{II}(\eta^6\text{-}C_6Me_6)(H)](CF_3SO_3)$ [55]. The counter anions are omitted for clarity (Reprinted with the permission from Ref. [55, 109]. Copyright 2003 American Chemical Society)

over $[\mathbf{Ir^B}\text{–}OH]^-$ and HCO_3^- over CO_3^{2-} (red line and red dashed line in Fig. 11.17, respectively). Thus, the reduction of HCO_3^- by H_2 is catalyzed by $[\mathbf{Ir^B}\text{–}H_2O]^0$ at pH 8.8. The TOF value at pH 8.8 increased linearly with increasing concentration of CO_2, which is converted to mixture of HCO_3^- and CO_3^{2-} (Fig. 11.18) [66]. Thus, the rate-determining step in the catalytic reduction of CO_2 to formate by H_2 is the insertion of CO_2 to the Ir–H complex $[\mathbf{Ir^B}\text{–}H]^0$ to produce the formate complex in Scheme 11.16 [66].

A dinuclear Cp*Ir catalyst with 4,4,6,6-tetrahydroxy-2,2-bipyrimidine as a bridging ligand (see the crystal structure in Fig. 11.19) can also catalyze the reduction of CO_2 by H_2 at ambient pressure at pH 8.4 with $\text{TOF} = 70\ h^{-1}$ at 298 K [110]. Mononuclear Cp*Ir complexes with biazole ligands also act as

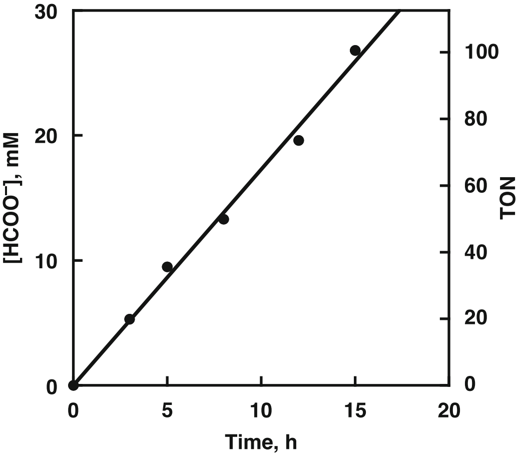

Fig. 11.16 Time course of the concentration of formate and TON for the formate formation in the reduction of CO_2 by H_2 catalyzed by $[\mathbf{Ir^B}–H_2O]^0$ (0.26 mM) under atmospheric pressure of H_2 (50 mL/min) and CO_2 (50 mL/min) in deaerated H_2O at 303 K at pH 7.5 (Reproduced from Ref. [66] by permission of The Royal Society of Chemistry)

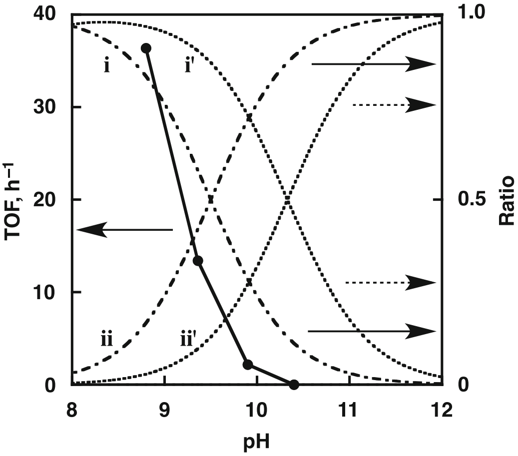

Fig. 11.17 pH dependence of the formation rate (TOF) of formate in the catalytic generation of formate from H_2, HCO_3^-, and CO_3^{2-} ($[HCO_3^-]+[CO_3^{2-}]=2.0$ M) catalyzed by $[\mathbf{Ir^B}–H_2O]^0$ (0.18 mM) in deaerated H_2O at 333 K (*solid line*). Alternate *long* and *short dashed lines*, (*i*) and (*ii*) show the amount ratios of complex $[\mathbf{Ir^B}–H_2O]^0$ and $[\mathbf{Ir^B}–OH]^-$, respectively, to the total amount of these complexes. *Dashed lines*, (*i′*) and (*ii′*) show the ratios of HCO_3^- and CO_3^{2-}, respectively (Reproduced from Ref. [66] by permission of The Royal Society of Chemistry)

efficient catalysts for reduction of CO_2 by H_2 to formate at ambient pressure and temperature [111].

Iridium complexes mentioned above act as efficient catalysts for the selective decomposition of formic acid to H_2 and CO_2 without formation of CO under acidic conditions at ambient temperature [55, 66, 110, 111]. Thus, the catalytic interconversion between hydrogen and formic acid has been made possible by changing pH

Fig. 11.18 Plot of TOF vs. the concentration of $KHCO_3$ and K_2CO_3 mixture ($KHCO_3/K_2CO_3$), i.e., $[KHCO_3] + [K_2CO_3]$ in the hydrogenation reaction of $KHCO_3/K_2CO_3$ with H_2 catalyzed by $[\mathbf{Ir^B}–H_2O]^0$ (0.18 mM) under atmospheric pressure of H_2 in deaerated H_2O at pH 8.8 at 333 K (Reproduced from Ref. [66] by permission of The Royal Society of Chemistry)

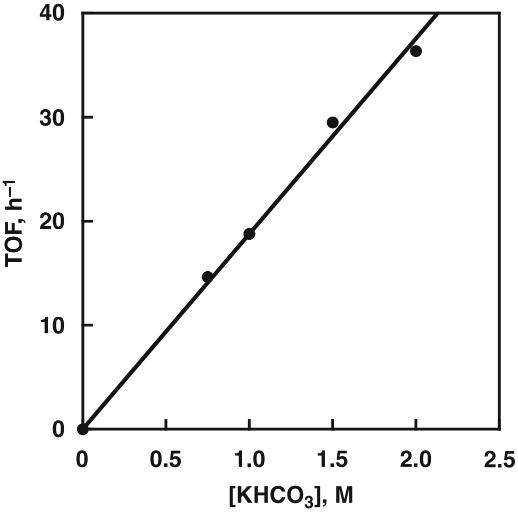

Scheme 11.16 Catalytic mechanism of CO_2 reduction by H_2 with $[\mathbf{Ir^A}–H_2O]^+$ to form $HCOO^-$ in H_2O

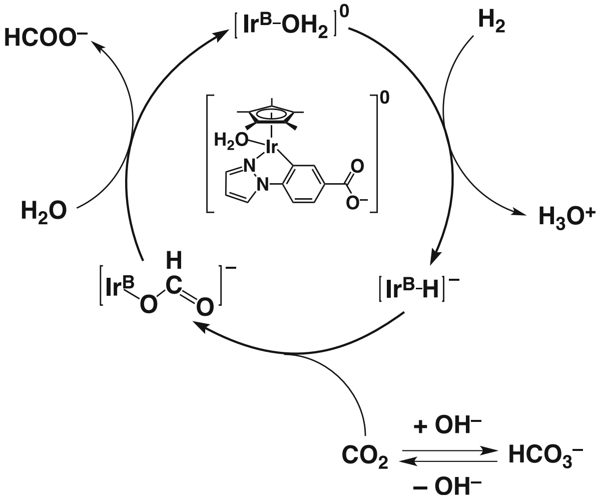

with the same catalyst, providing a convenient hydrogen-on-demand system in which hydrogen (gas) can be stored as formic acid (liquid) and whenever needed hydrogen is produced by the catalytic decomposition of formic acid [11, 66, 112]. Formic acid can also be directly used as a fuel in direct formic acid fuel cells, which have recently attracted much attention due to high electromotive force, limited fuel crossover, and high practical power densities at low temperatures as compared with direct methanol fuel cells [113–116].

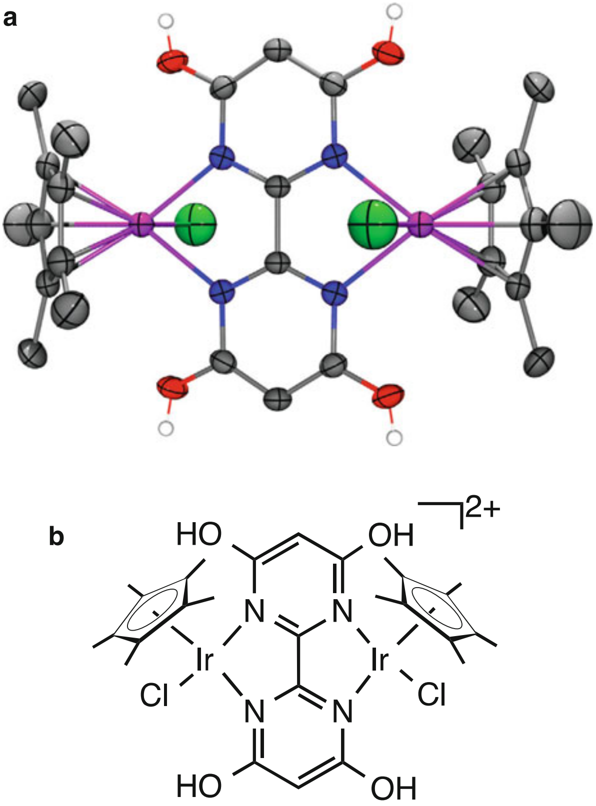

Fig. 11.19 (**a**) X-ray crystal structure and (**b**) the structural formula of a dinuclear Cp^*Ir catalyst with 4,4,6,6-tetrahydroxy-2,2-bipyrimidine as a bridging ligand employed for efficient CO_2 reduction to formate by H_2 (Reprinted by permission from Macmillan Publishers Ltd: Ref. [110], copyright 2012)

11.3 Conclusions

We have overviewed kinetic studies on catalytic reduction of protons and CO_2 in mainly homogeneous phase, providing valuable mechanistic insights. Kinetic studies including deuterium kinetic isotope effects on heterogeneous catalysts for hydrogen evolution have also been demonstrated to provide essential mechanistic information on bond cleavage and formation associated with electron transfer. Kinetic studies have also enabled us to determine the rate-determining steps in the catalytic cycles, providing valuable information on observable intermediates, which can be detected by various methods. The most important intermediates in the catalytic reduction of protons and CO_2 are metal-hydride complexes, which can reduce protons and CO_2 to produce hydrogen and formic acid, respectively. Metal η^1-CO_2 complexes that are formed by a nucleophilic attack to low-valent metal complexes with the central carbon are responsible for the two-electron reduction of CO_2 to CO [33, 99, 117–119]. The key remaining challenge is not just two-electron reduction of CO_2 with two protons to formic acid or carbon monoxide (CO) but multiple proton-coupled electron transfers to produce further reduced products such as methanol and methane. Such multi-electron reduction beyond two-electron reduction of CO_2 has so far been achieved in the heterogeneous systems by photocatalysis and electrocatalysis [13, 16, 120–132]. A series of different homogeneous catalysts have also been employed to achieve the catalytic reduction of CO_2 by H_2 to methanol in a single vessel to promote the various steps of the CO_2 reduction sequence [133]. Recently the homogenously catalyzed reduction of CO_2 by H_2 to methanol has been achieved by a single ruthenium phosphine complex [134, 135]. Methanol can also be obtained by the disproportion of formic acid catalyzed by an Ir complex ($[Ir^{III}(Cp^*)(bpy)(H_2O)](OTf)_2$) [136]. Further kinetic studies on such homogeneously catalyzed multi-electron reduction of CO_2 by H_2 may elucidate the catalytic mechanisms, which will certainly help develop efficient catalysts for production of carbon-neutral alternatives to fossil fuels.

Acknowledgements The authors gratefully acknowledge the contributions of their collaborators and coworkers cited in the references and support by an ALCA (Advanced Low Carbon Technology Research and Development) program from the Japan Science and Technology Agency and funds from the Ministry of Education, Culture, Sports, Science, and Technology, Japan.

References

1. Lewis NS, Nocera DG (2006) Powering the planet: chemical challenges in solar energy utilization. Proc Natl Acad Sci U S A 103:15729–15735
2. Gray HB (2009) Powering the planet with solar fuel. Nat Chem 1:7–7
3. Thomas JM (2014) Reflections on the topic of solar fuels. Energy Environ Sci 7:19–20
4. Faunce TA, Lubitz W, Rutherford AW, MacFarlane D, Moore GF, Yang P, Nocera DG, Moore TA, Gregory DH, Fukuzumi S, Yoon KB, Armstrong FA, Wasielewski MR, Styring S (2013) Energy and environment policy case for a global project on artificial photosynthesis. Energy Environ Sci 6:695–698
5. Züttel A, Borgschulte A, Schlapbach L (eds) (2011) Hydrogen as a future energy carrier. Wiley-VCH, Weinheim
6. Nocera DG (2012) The artificial leaf. Acc Chem Res 45:767–776
7. Kärkäs MD, Johnston EV, Verho O, Åkermark B (2013) Artificial photosynthesis: from nanosecond electron transfer to catalytic water oxidation. Acc Chem Res 47:100–111
8. Wen F, Li C (2013) Hybrid artificial photosynthetic systems comprising semiconductors as light harvesters and biomimetic complexes as molecular cocatalysts. Acc Chem Res 46:2355–2364
9. Bensaid S, Centi G, Garrone E, Perathoner S, Saracco G (2012) Towards artificial leaves for solar hydrogen and fuels from carbon dioxide. ChemSusChem 5:500–521
10. Fukuzumi S, Hong D, Yamada Y (2013) Bioinspired photocatalytic water reduction and oxidation with earth-abundant metal catalysts. J Phys Chem Lett 4:3458–3467
11. Fukuzumi S (2008) Bioinspired energy conversion systems for hydrogen production and storage. Eur J Inorg Chem 2008:1351–1362
12. Balzani V, Credi A, Venturi M (2008) Photochemical conversion of solar energy. ChemSusChem 1:26–58
13. Habisreutinger SN, Schmidt-Mende L, Stolarczyk JK (2013) Photocatalytic reduction of CO_2 on TiO_2 and other semiconductors. Angew Chem Int Ed 52:7372–7408

14. Liao F, Zeng Z, Eley C, Lu Q, Hong X, Tsang SCE (2012) Electronic modulation of a copper/zinc oxide catalyst by a heterojunction for selective hydrogenation of carbon dioxide to methanol. Angew Chem Int Ed 51:5832–5836
15. Benson EE, Kubiak CP, Sathrum AJ, Smieja JM (2009) Electrocatalytic and homogeneous approaches to conversion of CO_2 to liquid fuels. Chem Soc Rev 38:89–99
16. Liu Q, Wu D, Zhou Y, Su H, Wang R, Zhang C, Yan S, Xiao M, Zou Z (2014) Single-crystalline, ultrathin $ZnGa_2O_4$ nanosheet scaffolds to promote photocatalytic activity in CO_2 reduction into methane. ACS Appl Mater Interfaces 6:2356–2361
17. Wasielewski MR (2009) Self-assembly strategies for integrating light harvesting and charge separation in artificial photosynthetic systems. Acc Chem Res 42:1910–1921
18. Gust D, Moore TA, Moore AL (2009) Solar fuels via artificial photosynthesis. Acc Chem Res 42:1890–1898
19. Guldi DM, Sgobba V (2011) Carbon nanostructures for solar energy conversion schemes. Chem Commun 47:606–610
20. Fukuzumi S (2008) Development of bioinspired artificial photosynthetic systems. PCCP 10:2283–2297
21. D'Souza F, Ito O (2012) Photosensitized electron transfer processes of nanocarbons applicable to solar cells. Chem Soc Rev 41:86–96
22. Fukuzumi S, Ohkubo K (2012) Assemblies of artificial photosynthetic reaction centres. J Mater Chem 22:4575–4587
23. Fukuzumi S, Ohkubo K, Suenobu T (2014) Long-lived charge separation and applications in artificial photosynthesis. Acc Chem Res 47:1455–1464
24. Fukuzumi S, Yamada Y, Suenobu T, Ohkubo K, Kotani H (2011) Catalytic mechanisms of hydrogen evolution with homogeneous and heterogeneous catalysts. Energy Environ Sci 4:2754–2766
25. Fukuzumi S, Yamada Y (2012) Catalytic activity of metal-based nanoparticles for photocatalytic water oxidation and reduction. J Mater Chem 22:24284–24296
26. Dempsey JL, Brunschwig BS, Winkler JR, Gray HB (2009) Hydrogen evolution catalyzed by cobaloximes. Acc Chem Res 42:1995–2004
27. Eckenhoff WT, Eisenberg R (2012) Molecular systems for light driven hydrogen production. Dalton Trans 41:13004–13021
28. Halpin Y, Pryce MT, Rau S, Dini D, Vos JG (2013) Recent progress in the development of bimetallic photocatalysts for hydrogen generation. Dalton Trans 42:16243–16254
29. Schneider J, Jia H, Muckerman JT, Fujita E (2012) Thermodynamics and kinetics of CO_2, CO, and H^+ binding to the metal centre of CO_2 reduction catalysts. Chem Soc Rev 41:2036–2051
30. Schulz M, Karnahl M, Schwalbe M, Vos JG (2012) The role of the bridging ligand in photocatalytic supramolecular assemblies for the reduction of protons and carbon dioxide. Coord Chem Rev 256:1682–1705
31. Fukuzumi S, Suenobu T (2013) Hydrogen storage and evolution catalysed by metal hydride complexes. Dalton Trans 42:18–28
32. Jessop PG, Joó F, Tai C-C (2004) Recent advances in the homogeneous hydrogenation of carbon dioxide. Coord Chem Rev 248:2425–2442
33. Kobayashi K, Tanaka K (2014) Approach to multi-electron reduction beyond two-electron reduction of CO_2. Phys Chem Chem Phys 16:2240–2250
34. Concepcion JJ, Jurss JW, Brennaman MK, Hoertz PG, Patrocinio AOT, Murakami Iha NY, Templeton JL, Meyer TJ (2009) Making oxygen with ruthenium complexes. Acc Chem Res 42:1954–1965
35. Sala X, Maji S, Bofill R, García-Antón J, Escriche L, Llobet A (2013) Molecular water oxidation mechanisms followed by transition metals: state of the art. Acc Chem Res 47:504–516
36. Meyer TJ, Huynh MHV (2003) The remarkable reactivity of high oxidation state ruthenium and osmium polypyridyl complexes. Inorg Chem 42:8140–8160

37. Lv H, Geletii YV, Zhao C, Vickers JW, Zhu G, Luo Z, Song J, Lian T, Musaev DG, Hill CL (2012) Polyoxometalate water oxidation catalysts and the production of green fuel. Chem Soc Rev 41:7572–7589
38. Liu X, Wang F (2012) Transition metal complexes that catalyze oxygen formation from water: 1979–2010. Coord Chem Rev 256:1115–1136
39. Cao R, Lai W, Du P (2012) Catalytic water oxidation at single metal sites. Energy Environ Sci 5:8134–8157
40. Singh A, Spiccia L (2013) Water oxidation catalysts based on abundant 1st row transition metals. Coord Chem Rev 257:2607–2622
41. Cady CW, Crabtree RH, Brudvig GW (2008) Functional models for the oxygen-evolving complex of photosystem II. Coord Chem Rev 252:444–455
42. Duan L, Tong L, Xu Y, Sun L (2011) Visible light-driven water oxidation-from molecular catalysts to photoelectrochemical cells. Energy Environ Sci 4:3296–3313
43. Le Goff A, Artero V, Jousselme B, Tran PD, Guillet N, Métayé R, Fihri A, Palacin S, Fontecave M (2009) From hydrogenases to noble metal–free catalytic nanomaterials for H_2 production and uptake. Science 326:1384–1387
44. Thoi VS, Sun Y, Long JR, Chang CJ (2013) Complexes of earth-abundant metals for catalytic electrochemical hydrogen generation under aqueous conditions. Chem Soc Rev 42:2388–2400
45. Wang M, Chen L, Sun L (2012) Recent progress in electrochemical hydrogen production with earth-abundant metal complexes as catalysts. Energy Environ Sci 5:6763–6778
46. Losse S, Vos JG, Rau S (2010) Catalytic hydrogen production at cobalt centres. Coord Chem Rev 254:2492–2504
47. Esswein AJ, Nocera DG (2007) Hydrogen production by molecular photocatalysis. Chem Rev 107:4022–4047
48. Wang M, Na Y, Gorlov M, Sun L (2009) Light-driven hydrogen production catalysed by transition metal complexes in homogeneous systems. Dalton Trans 2009:6458–6467
49. Mandal S, Shikano S, Yamada Y, Lee Y-M, Nam W, Llobet A, Fukuzumi S (2013) Protonation equilibrium and hydrogen production by a dinuclear cobalt–hydride complex reduced by cobaltocene with trifluoroacetic acid. J Am Chem Soc 135:15294–15297
50. Varma S, Castillo CE, Stoll T, Fortage J, Blackman AG, Molton F, Deronzier A, Collomb M-N (2013) Efficient photocatalytic hydrogen production in water using a cobalt(III) tetraaza-macrocyclic catalyst: electrochemical generation of the low-valent Co(I) species and its reactivity toward proton reduction. Phys Chem Chem Phys 15:17544–17552
51. Guttentag M, Rodenberg A, Kopelent R, Probst B, Buchwalder C, Brandstätter M, Hamm P, Alberto R (2012) Photocatalytic H_2 production with a rhenium/cobalt system in water under acidic conditions. Eur J Inorg Chem 2012:59–64
52. Krishnan CV, Brunschwig BS, Creutz C, Sutin N (1985) Homogeneous catalysis of the photoreduction of water. 6. Mediation by polypyridine complexes of ruthenium(II) and cobalt (II) in alkaline media. J Am Chem Soc 107:2005–2015
53. Krishnan CV, Sutin N (1981) Homogeneous catalysis of the photoreduction of water by visible light. 2. Mediation by a tris(2,2′-bipyridine)ruthenium(II)-cobalt(II) bipyridine system. J Am Chem Soc 103:2141–2142
54. Fukuzumi S, Kobayashi T, Suenobu T (2008) Efficient catalytic decomposition of formic acid for the selective generation of H_2 and H/D exchange with a water-soluble rhodium complex in aqueous solution. ChemSusChem 1:827–834
55. Abura T, Ogo S, Watanabe Y, Fukuzumi S (2003) Isolation and crystal structure of a water-soluble iridium hydride: a robust and highly active catalyst for acid-catalyzed transfer hydrogenations of carbonyl compounds in acidic media. J Am Chem Soc 125:4149–4154
56. Suenobu T, Guldi DM, Ogo S, Fukuzumi S (2003) Excited-state deprotonation and H/D exchange of an iridium hydride complex. Angew Chem Int Ed 42:5492–5495

57. Fukuzumi S, Kobayashi T, Suenobu T (2011) Photocatalytic production of hydrogen by disproportionation of one-electron-reduced rhodium and iridium–ruthenium complexes in water. Angew Chem Int Ed 50:728–731
58. Stoll T, Gennari M, Serrano I, Fortage J, Chauvin J, Odobel F, Rebarz M, Poizat O, Sliwa M, Deronzier A, Collomb M-N (2013) $[Rh^{III}(dmbpy)_2Cl_2]^+$ as a highly efficient catalyst for visible-light-driven hydrogen production in pure water: comparison with other rhodium catalysts. Chem Eur J 19:782–792
59. Amouyal E, Koffi P (1985) Photochemical production of hydrogen from water. J Photochem 29:227–242
60. Weddle KS, Aiken JD, Finke RG (1998) Rh(0) nanoclusters in benzene hydrogenation catalysis: kinetic and mechanistic evidence that a putative $[(C_8H_{17})_3NCH_3]^+[RhCl_4]^-$-ion-pair catalyst is actually a distribution of Cl^- and $[(C_8H_{17})_3NCH_3]^+$ stabilized Rh (0) nanoclusters. J Am Chem Soc 120:5653–5666
61. Fukuzumi S, Kobayashi T, Suenobu T (2010) Unusually large tunneling effect on highly efficient generation of hydrogen and hydrogen isotopes in pH-selective decomposition of formic acid catalyzed by a heterodinuclear iridium-ruthenium complex in water. J Am Chem Soc 132:1496–1497
62. Kwart H (1982) Temperature dependence of the primary kinetic hydrogen isotope effect as a mechanistic criterion. Acc Chem Res 15:401–408
63. Bercaw JE, Chen GS, Labinger JA, Lin B-L (2008) Hydrogen tunneling in protonolysis of platinum(II) and palladium(II) methyl complexes: mechanistic implications. J Am Chem Soc 130:17654–17655
64. Pan Z, Horner JH, Newcomb M (2008) Tunneling in C – H oxidation reactions by an oxoiron (IV) porphyrin radical cation: direct measurements of very large H/D kinetic isotope effects. J Am Chem Soc 130:7776–7777
65. Kohen A, Klinman JP (1998) Enzyme catalysis: beyond classical paradigms. Acc Chem Res 31:397–404
66. Maenaka Y, Suenobu T, Fukuzumi S (2012) Catalytic interconversion between hydrogen and formic acid at ambient temperature and pressure. Energy Environ Sci 5:7360–7367
67. Ruelle P, Kesselring UW, Ho N-T (1986) Ab initio quantum-chemical study of the unimolecular pyrolysis mechanisms of formic acid. J Am Chem Soc 108:371–375
68. Dau H, Haumann M (2008) The manganese complex of photosystem II in its reaction cycle-basic framework and possible realization at the atomic level. Coord Chem Rev 252:273–295
69. Maenaka Y, Suenobu T, Fukuzumi S (2011) Efficient catalytic interconversion between NADH and NAD^+ accompanied by generation and consumption of hydrogen with a water-soluble iridium complex at ambient pressure and temperature. J Am Chem Soc 134:367–374
70. Kotani H, Ono T, Ohkubo K, Fukuzumi S (2007) Efficient photocatalytic hydrogen evolution without an electron mediator using a simple electron donor-acceptor dyad. Phys Chem Chem Phys 9:1487–1492
71. Hasobe T, Sakai H, Mase K, Ohkubo K, Fukuzumi S (2013) Remarkable enhancement of photocatalytic hydrogen evolution efficiency utilizing an internal cavity of supramolecular porphyrin hexagonal nanocylinders under visible-light irradiation. J Phys Chem C 117:4441–4449
72. Yamada Y, Miyahigashi T, Kotani H, Ohkubo K, Fukuzumi S (2012) Photocatalytic hydrogen evolution with Ni nanoparticles by using 2-phenyl-4-(1-naphthyl)quinolinium ion as a photocatalyst. Energy Environ Sci 5:6111–6118
73. Amao Y (2011) Solar fuel production based on the artificial photosynthesis system. ChemCatChem 3:458–474
74. Maenaka Y, Suenobu T, Fukuzumi S (2012) Hydrogen evolution from aliphatic alcohols and 1,4-selective hydrogenation of NAD^+ catalyzed by a C, N and a C, C cyclometalated organoiridium complex at room temperature in water. J Am Chem Soc 134:9417–9427
75. Nielsen M, Alberico E, Baumann W, Drexler H-J, Junge H, Gladiali S, Beller M (2013) Low-temperature aqueous-phase methanol dehydrogenation to hydrogen and carbon dioxide. Nature 495:85–89

76. Monney A, Barsch E, Sponholz P, Junge H, Ludwig R, Beller M (2014) Base-free hydrogen generation from methanol using a bi-catalytic system. Chem Commun 50:707–709
77. Chen Z, Glasson CRK, Holland PL, Meyer TJ (2013) Electrogenerated polypyridyl ruthenium hydride and ligand activation for water reduction to hydrogen and acetone to iso-propanol. Phys Chem Chem Phys 15:9503–9507
78. Bullock RM, Appel AM, Helm ML (2014) Production of hydrogen by electrocatalysis: making the H-H bond by combining protons and hydrides. Chem Commun 50:3125–3143
79. Chen S, Ho M-H, Bullock RM, DuBois DL, Dupuis M, Rousseau R, Raugei S (2014) Computing free energy landscapes: application to Ni-based electrocatalysts with pendant amines for H_2 production and oxidation. ACS Catal 4:229–242
80. Raugei S, Chen S, Ho M-H, Ginovska-Pangovska B, Rousseau RJ, Dupuis M, DuBois DL, Bullock RM (2012) The role of pendant amines in the breaking and forming of molecular hydrogen catalyzed by nickel complexes. Chem Eur J 18:6493–6506
81. Rose MJ, Gray HB, Winkler JR (2012) Hydrogen generation catalyzed by fluorinated diglyoxime-iron complexes at low overpotentials. J Am Chem Soc 134:8310–8313
82. Helm ML, Stewart MP, Bullock RM, DuBois MR, DuBois DL (2011) A synthetic nickel electrocatalyst with a turnover frequency above 100,000 s^{-1} for H_2 production. Science 333:863–866
83. DuBois DL (2014) Development of molecular electrocatalysts for energy storage. Inorg Chem 53:3935–3960
84. Fukuzumi S, Kotani H, Ohkubo K, Ogo S, Tkachenko NV, Lemmetyinen H (2004) Electron-transfer state of 9-mesityl-10-methylacridinium ion with a much longer lifetime and higher energy than that of the natural photosynthetic reaction center. J Am Chem Soc 126:1600–1601
85. Kotani H, Hanazaki R, Ohkubo K, Yamada Y, Fukuzumi S (2011) Size- and shape-dependent activity of metal nanoparticles as hydrogen-evolution catalysts: mechanistic insights into photocatalytic hydrogen evolution. Chem Eur J 17:2777–2785
86. Ohkubo K, Kotani H, Fukuzumi S (2005) Misleading effects of impurities derived from the extremely long-lived electron-transfer state of 9-mesityl-10-methylacridinium ion. Chem Commun 2005:4520–4522
87. Fukuzumi S, Kotani H, Ohkubo K (2008) Response: why had long-lived electron-transfer states of donor-substituted 10-methylacridinium ions been overlooked? Formation of the dimer radical cations detected in the near-IR region. Phys Chem Chem Phys 10:5159–5162
88. Hoshino M, Uekusa H, Tomita A, Koshihara S, Sato T, Nozawa S, Adachi S, Ohkubo K, Kotani H, Fukuzumi S (2012) Determination of the structural features of a long-lived-electron-transfer state of 9-mesityl-10-methylacridinium ion. J Am Chem Soc 134:4569–4572
89. Kotani H, Ohkubo K, Fukuzumi S (2012) Formation of a long-lived electron-transfer state of a naphthalene-quinolinium ion dyad and the π-dimer radical cation. Faraday Discuss 155:89–102
90. Yamada Y, Miyahigashi T, Kotani H, Ohkubo K, Fukuzumi S (2011) Photocatalytic hydrogen evolution under highly basic conditions by using Ru nanoparticles and 2-phenyl-4-(1-naphthyl)quinolinium ion. J Am Chem Soc 133:16136–16145
91. Aresta M, Dibenedetto A, Angelini A (2014) Catalysis for the valorization of exhaust carbon: from CO_2 to chemicals, materials, and fuels. Technological use of CO_2. Chem Rev 114:1709–1742
92. Saeidi S, Amin NAS, Rahimpour MR (2014) Hydrogenation of CO_2 to value-added-products—a review and potential future developments. J CO_2 Util 5:66–81
93. Wang W, Wang S, Ma X, Gong J (2011) Recent advances in catalytic hydrogenation of carbon dioxide. Chem Soc Rev 40:3703–3727
94. Kondratenko EV, Mul G, Baltrusaitis J, Larrazabal GO, Perez-Ramirez J (2013) Status and perspectives of CO_2 conversion into fuels and chemicals by catalytic, photocatalytic and electrocatalytic processes. Energy Environ Sci 6:3112–3135
95. Centi G, Quadrelli EA, Perathoner S (2013) Catalysis for CO_2 conversion: a key technology for rapid introduction of renewable energy in the value chain of chemical industries. Energy Environ Sci 6:1711–1731

96. Olah GA, Goeppert A, Prakash GKS (2009) Chemical recycling of carbon dioxide to methanol and dimethyl ether: from greenhouse gas to renewable, environmentally carbon neutral fuels and synthetic hydrocarbons. J Org Chem 74:487–498
97. Jessop PG, Ikariya T, Noyori R (1994) Homogeneous catalytic-hydrogenation of supercritical carbon-dioxide. Nature 368:231–233
98. Jessop PG, Ikariya T, Noyori R (1995) Homogeneous hydrogenation of carbon-dioxide. Chem Rev 95:259–272
99. Tanaka K, Ooyama D (2002) Multi-electron reduction of CO_2 via Ru-CO_2, -C(O)OH, -CO, -CHO, and -CH_2OH species. Coord Chem Rev 226:211–218
100. Wesselbaum S, Hintermair U, Leitner W (2012) Continuous-flow hydrogenation of carbon dioxide to pure formic acid using an integrated scCO_2 process with immobilized catalyst and base. Angew Chem Int Ed 51:8585–8588
101. Ziebart C, Federsel C, Anbarasan P, Jackstell R, Baumann W, Spannenberg A, Beller M (2012) Well-defined iron catalyst for improved hydrogenation of carbon dioxide and bicarbonate. J Am Chem Soc 134:20701–20704
102. Jeletic MS, Mock MT, Appel AM, Linehan JC (2013) A cobalt-based catalyst for the hydrogenation of CO_2 under ambient conditions. J Am Chem Soc 135:11533–11536
103. Huff CA, Sanford MS (2013) Catalytic CO_2 hydrogenation to formate by a ruthenium pincer complex. ACS Catal 3:2412–2416
104. Li Y-N, He L-N, Liu A-H, Lang X-D, Yang Z-Z, Yu B, Luan C-R (2013) In situ hydrogenation of captured CO_2 to formate with polyethyleneimine and Rh/monophosphine system. Green Chem 15:2825–2829
105. Drake JL, Manna CM, Byers JA (2013) Enhanced carbon dioxide hydrogenation facilitated by catalytic quantities of bicarbonate and other inorganic salts. Organometallics 32:6891–6894
106. Badiei YM, Wang W-H, Hull JF, Szalda DJ, Muckerman JT, Himeda Y, Fujita E (2013) Cp*Co(III) catalysts with proton-responsive ligands for carbon dioxide hydrogenation in aqueous media. Inorg Chem 52:12576–12586
107. Ogo S, Kabe R, Hayashi H, Harada R, Fukuzumi S (2006) Mechanistic investigation of CO_2 hydrogenation by Ru(II) and Ir(III) aqua complexes under acidic conditions: two catalytic systems differing in the nature of the rate determining step. Dalton Trans 4657–4663
108. Hayashi H, Ogo S, Fukuzumi S (2004) Aqueous hydrogenation of carbon dioxide catalysed by water-soluble ruthenium aqua complexes under acidic conditions. Chem Commun 2004:2714–2715
109. Hayashi H, Ogo S, Abura T, Fukuzumi S (2003) Accelerating effect of a proton on the reduction of CO_2 dissolved in water under acidic conditions. Isolation, crystal structure, and reducing ability of a water-soluble ruthenium hydride complex. J Am Chem Soc 125:14266–14267
110. Hull JF, Himeda Y, Wang W-H, Hashiguchi B, Periana R, Szalda DJ, Muckerman JT, Fujita E (2012) Reversible hydrogen storage using CO_2 and a proton-switchable iridium catalyst in aqueous media under mild temperatures and pressures. Nat Chem 4:383–388
111. Manaka Y, Wang W-H, Suna Y, Kambayashi H, Muckerman JT, Fujita E, Himeda Y (2014) Efficient H_2 generation from formic acid using azole complexes in water. Catal Sci Technol 4:34–37
112. Fujita E, Muckerman JT, Himeda Y (2013) Interconversion of CO_2 and formic acid by bio-inspired Ir complexes with pendent bases. Biochim Biophys Acta Bioenerg 1827:1031–1038
113. Ge J, Chen X, Liu C, Lu T, Liao J, Liang L, Xing W (2010) Promoting effect of vanadium ions on the anodic Pd/C catalyst for direct formic acid fuel cell application. Electrochim Acta 55:9132–9136
114. Wang R, Liu J, Liu P, Bi X, Yan X, Wang W, Ge X, Chen M, Ding Y (2014) Dispersing Pt atoms onto nanoporous gold for high performance direct formic acid fuel cells. Chem Sci 5:403–409
115. Cai W, Liang L, Zhang Y, Xing W, Liu C (2013) Real contribution of formic acid in direct formic acid fuel cell: investigation of origin and guiding for micro structure design. Int J Hydrog Energy 38:212–218

116. Ji X, Lee KT, Holden R, Zhang L, Zhang J, Botton GA, Couillard M, Nazar LF (2010) Nanocrystalline intermetallics on mesoporous carbon for direct formic acid fuel cell anodes. Nat Chem 2:286–293
117. Morris AJ, Meyer GJ, Fujita E (2009) Molecular approaches to the photocatalytic reduction of carbon dioxide for solar fuels. Acc Chem Res 42:1983–1994
118. Takeda H, Ishitani O (2010) Development of efficient photocatalytic systems for CO_2 reduction using mononuclear and multinuclear metal complexes based on mechanistic studies. Coord Chem Rev 254:346–354
119. Chen Z, Concepcion JJ, Brennaman MK, Kang P, Norris MR, Hoertz PG, Meyer TJ (2012) Splitting CO_2 into CO and O_2 by a single catalyst. Proc Natl Acad Sci U S A 109:15606–15611
120. Izumi Y (2013) Recent advances in the photocatalytic conversion of carbon dioxide to fuels with water and/or hydrogen using solar energy and beyond. Coord Chem Rev 257:171–186
121. Yan S, Wang J, Zou Z (2013) An anion-controlled crystal growth route to Zn_2GeO_4 nanorods for efficient photocatalytic conversion of CO_2 into CH_4. Dalton Trans 42:12975–12979
122. Roy SC, Varghese OK, Paulose M, Grimes CA (2010) Toward solar fuels: photocatalytic conversion of carbon dioxide to hydrocarbons. ACS Nano 4:1259–1278
123. Hamdy MS, Amrollahi R, Sinev I, Mei B, Mul G (2014) Strategies to design efficient silica-supported photocatalysts for reduction of CO_2. J Am Chem Soc 136:594–597
124. Yu J, Jin J, Cheng B, Jaroniec M (2014) A noble metal-free reduced graphene oxide-CdS nanorod composite for the enhanced visible-light photocatalytic reduction of CO_2 to solar fuel. J Mater Chem A 2:3407–3416
125. Andrews E, Ren M, Wang F, Zhang Z, Sprunger P, Kurtz R, Flake J (2013) Electrochemical reduction of CO_2 at Cu nanocluster/$(10\hat{1}0)$ ZnO electrodes. J Electrochem Soc 160:H841–H846
126. Le M, Ren M, Zhang Z, Sprunger PT, Kurtz RL, Flake JC (2011) Electrochemical reduction of CO_2 to CH_3OH at copper oxide surfaces. J Electrochem Soc 158:E45–E49
127. Schouten KJP, Kwon Y, van der Ham CJM, Qin Z, Koper MTM (2011) A new mechanism for the selectivity to C-1 and C-2 species in the electrochemical reduction of carbon dioxide on copper electrodes. Chem Sci 2:1902–1909
128. Costentin C, Robert M, Savéant J-M (2013) Catalysis of the electrochemical reduction of carbon dioxide. Chem Soc Rev 42:2423–2436
129. Qiao J, Liu Y, Hong F, Zhang J (2014) A review of catalysts for the electroreduction of carbon dioxide to produce low-carbon fuels. Chem Soc Rev 43:631–675
130. Peterson AA, Nørskov JK (2012) Activity descriptors for CO_2 electroreduction to methane on transition-metal catalysts. J Phys Chem Lett 3:251–258
131. Yan Y, Zeitler EL, Gu J, Hu Y, Bocarsly AB (2013) Electrochemistry of aqueous pyridinium: exploration of a key aspect of electrocatalytic reduction of CO_2 to methanol. J Am Chem Soc 135:14020–14023
132. Cole EB, Lakkaraju PS, Rampulla DM, Morris AJ, Abelev E, Bocarsly AB (2010) Using a one-electron shuttle for the multielectron reduction of CO_2 to methanol: kinetic, mechanistic, and structural insights. J Am Chem Soc 132:11539–11551
133. Huff CA, Sanford MS (2011) Cascade catalysis for the homogeneous hydrogenation of CO_2 to methanol. J Am Chem Soc 133:18122–18125
134. Wesselbaum S, vom Stein T, Klankermayer J, Leitner W (2012) Hydrogenation of carbon dioxide to methanol by using a homogeneous ruthenium-phosphine catalyst. Angew Chem Int Ed 51:7499–7502
135. Li Y, Junge K, Beller M (2013) Improving the efficiency of the hydrogenation of carbonates and carbon dioxide to methanol. ChemCatChem 5:1072–1074
136. Miller AJM, Heinekey DM, Mayer JM, Goldberg KI (2013) Catalytic disproportionation of formic acid to generate methanol. Angew Chem Int Ed 52:3981–3984